

NUMERICAL PREDICTION OF PHASE SEPARATION IN TWO-PHASE FLOW THROUGH T-JUNCTIONS

R. I. ISSA and P. J. OLIVEIRA

Department of Mineral Resources Engineering, Imperial College of Science, Technology & Medicine,
 Prince Consort Road, London SW7 2BP, England

(Received 18 May 1992; in revised form 3 February 1993)

Abstract—The paper presents a predictive numerical method which solves the full, three-dimensional, two-fluid model equations for dispersed two-phase flow by control-volume discretization. The methodology incorporates general coordinates, indirect-addressing for easy mapping of non-rectangular domains and is based on the use of non-staggered meshes. Turbulence is modelled either by the standard k - ϵ turbulence model or by an extension of that model which accounts for void-fraction fluctuations. The method is applied to air–water bubbly flow in a rectangular cross-section T-junction for which experimental data is available. Comparisons of the predictions with measured velocities and phase separation ratios show good agreement. Contours of the volume-fraction reveal the presence of a pocket of high gas concentration at the entrance to the side arm, similar to that actually found in experiments. The effects of interfacial drag model, turbulence model and bubble diameter on the predictions are also investigated.

NOMENCLATURE

- | | |
|--|---|
| A —Coefficients in equations | U_i —Cartesian α -weighted velocity components |
| A_0 —Sum of neighbour coefficients | u_i —Instantaneous velocity component |
| A_p —Central coefficient in equations, equation (32) | u'_i —Unweighted velocity fluctuations ($u_i = \bar{u}_i + u'_i$) |
| A_p' —Coefficient equal to $A_p - A_0$, in Appendix | u''_i — α -Weighted velocity fluctuations ($u_i = U_i + u''_i$) |
| A_D —Drag factor [1/s], equation (6) | \bar{U}_f —Face-velocity at face f , equation (40) |
| B_{il} — i -Component of cell cross-section area along direction l | V_s —Slip velocity |
| B_f —Scalar area of cell face f | V —Volume of cell |
| C_D —Drag coefficient, equation (7) | W —Mass flow rate [kg/s] |
| C_i —Particle response function, equation (15) | x, y, z —Cartesian coordinates (x_i) |
| C_1, C_2, C_μ —Turbulence model constants; $C_1 = 1.44$; $C_2 = 1.92$; $C_\mu = 0.09$ | X, Y, Z —Non-dimensional x, y, z (X —along run; Y —along branch; Z —transverse) |
| D —Diffusion flux, equation (34) | x —Quality (gas mass fraction) |
| d —Diameter (of bubbles or particles) | X_R —Recirculation length in the side branch |
| $f(\alpha)$ —Drag corrective factor, dependent on α , equation (7) | α —Mean volume-fraction; void-fraction (i.e. gas volume-fraction). |
| E —Log-law constant, $E = 9.0$ | $\bar{\alpha}^f$ —Upwinded volume-fraction at face f |
| F —Cell index of neighbour cell across face f | β —Volumetric gas ratio, $Q_G/(Q_G + Q_L)$ |
| F —Mass convective fluxes [kg/s] | β_{ii} —Metric coefficients in coordinate transformation, equation (22) |
| F' —Convective flux divided by volume-fraction ($F' = F/\bar{\alpha}$) | δ_{ij} —Dirac delta |
| F_D —Drag parameter [kg/s/m ³], equation (35) | δt —Time step |
| g —Gravitational acceleration | Δ —Increment; difference between two volumes |
| G —Mass flux [kg/s/m ²], $G = W/A$ | ϵ —Rate of dissipation of k [m ² /s ³] |
| G —Generation of turbulence kinetic energy, equation (18) [kg/m/s ³] | ϕ —Generic variable |
| H —Operator denoting influence of neighbour cells, equation (35) | ρ —Density |
| J —Overall superficial velocities [m/s], $J = G/\rho$; Jacobian of transformation | σ_α —Prandtl number for α ($\sigma_\alpha = 1$) |
| k —Turbulence kinetic energy [m ² /s ²] | $\sigma_k, \sigma_\epsilon$ —Turbulent Schmidt numbers in the turbulence model: $\sigma_k = 1.0$; $\sigma_\epsilon = 1.22$ |
| K —Log-law constant, $K = 0.42$ | τ_{ij} —Shear stress |
| L, W, D —Dimensions: length, width and depth | μ —Dynamic viscosity [kg/m/s] |
| p —Pressure | μ^t —Eddy viscosity [kg/m/s] |
| p' —Pressure correction | ν —Kinematic viscosity [m ² /s] |
| P —Arbitrary cell index | ν^t —Eddy diffusivity [m ² /s] |
| Q —Volumetric flow rate [m ³ /s] | ξ, η, ζ —General coordinates; transformed coordinates |
| Re —Reynolds number | $\langle \cdot \rangle$ —Cross-sectional average |
| Re_b —Bubble or particle Reynolds number ($V_b d_b/\nu_c$) | |
| S —Source in equations | |
| t —Time | |
| t_c —Turbulence time scale, equation (15) | |
| t_p —Particle relaxation time, equation (15) | |

Subscripts

- 1, 2, 3—Inlet, run, branch in a T-junction
 α —Related with phase α or with volume-fraction
 b —Bubble

| | |
|---|--|
| c, d—Continuous and dispersed phase | <i>Superscripts</i> |
| ϵ —Related with turbulence (large eddies) | '—Time fluctuations |
| D—Drag | "— α -Weighted fluctuations |
| f —Situating at face f ; face | —Time average; arithmetic average |
| G, L—Gas and liquid | \wedge —Instantaneous value [used for α , equation (8)] |
| i, j, k —Indices of Cartesian coordinates (x_i) | *—Intermediate level in the algorithm, equations (47), . . . |
| l, k, m —Indices of general coordinates (ξ_i); directions along those coordinates | n —Time level |
| r —Relative (slip) | p —Pressure-correction equation coefficients, equation (49) |
| $(\cdot)_{,j}$ —Nabla, $\equiv \frac{\partial}{\partial x_j}$ | t—Turbulence related |
| | ef—Effective, molecular + turbulent |

INTRODUCTION

When a two-phase mixture flows through a T-junction, the phases tend to separate in different proportions among the outlet arms. The lighter phase, often gas, tends to be preferentially diverted into the side arm, while the heavier phase will flow straight through the main arm. As a consequence, the side arm of the dividing T-junction will carry a higher proportion of the gas than the straight arm, the value of which depends on an overall flow-rate split at the junction. It is clear that the design of equipment or processes downstream of the junction must therefore take such high variations in phase fractions in the arm into account. A method for the prediction of the degree of phase segregation is needed for this purpose.

Existing methods for predicting the flow split are either wholly empirical in nature [e.g. 1] or based on one-dimensional flow analysis still relying on empirical correlations. The latter methods define "zones of influence" [2, 3] or "dividing streamlines" [4] to determine the amount of gas flowing into the side branch. The zones of influence are the regions in the main-arm flow from which each phase is diverted into the branch. Hence, for the annular regime the zone of influence was defined geometrically [2] as the area formed by the intersection of the side arm with the circular sector encompassing it; the ratio of that area to the main pipe area would determine the proportion of gas drawn into the side arm, and the corresponding ratio of angles would determine the proportion of extracted liquid (from the film). Later, Azzopardi [5] introduced a correction for diameter ratios different from unity, and Azzopardi and Purvis [3] introduced a correction for the fraction of liquid entrained. In the dividing streamline approach the concept of zones of influence is still used, but these zones are now delineated by streamlines calculated from tangential and normal balances of centrifugal and interfacial drag forces. The shape of the dividing streamline for each phase is determined from its radius of curvature, which was empirically correlated from experimental data by Hwang *et al.* [4]; also, the distribution of one of the phases is required at the inlet pipe.

Hence, the above definitions are themselves derived from empirical findings thus rendering the predictability of phase separation to be still dependent on the particular experiment used to derive the relationships. In a review of the subject, Lahey [6] came to the conclusion that there exists no completely satisfactory model for predicting phase separation in conduits of untested geometries and operating conditions.

The present paper outlines a general three-dimensional calculation procedure based on the two-fluid model, and presents its application to the flow of bubbly two-phase mixtures through a dividing T-junction connecting rectangular cross-sectional channels. The procedure is based on the numerical solution of transport equations for momentum and continuity for each phase, together with additional equations pertaining to the $k-\epsilon$ turbulence model used to account for effects of turbulence. The finite-volume representation of T-junction geometries is facilitated by the use of block-structured computational meshes and an indirect-addressing technique.

For the purpose of validation of the method, comparisons are made where possible with data for dispersed flow. The following paragraphs provide a summary of available experimental data for phase separation in dividing T-junctions and discuss their relevance to the present work.

Azzopardi and co-workers have dealt mainly with flows in the annular regime, with low total mass fluxes ($G_1 \approx 50\text{--}150 \text{ kg/s/m}^2$) and where superficial velocities for the gas are quite high ($J_G \approx 5\text{--}40 \text{ m/s}$) and low for the liquid ($J_L \approx 0.01\text{--}9.1 \text{ m/s}$), resulting in high qualities, $x_1 \approx 30\text{--}90\%$. Measurements in vertical T-junctions are given in Refs [2, 3, 5]; for the horizontal case, where the

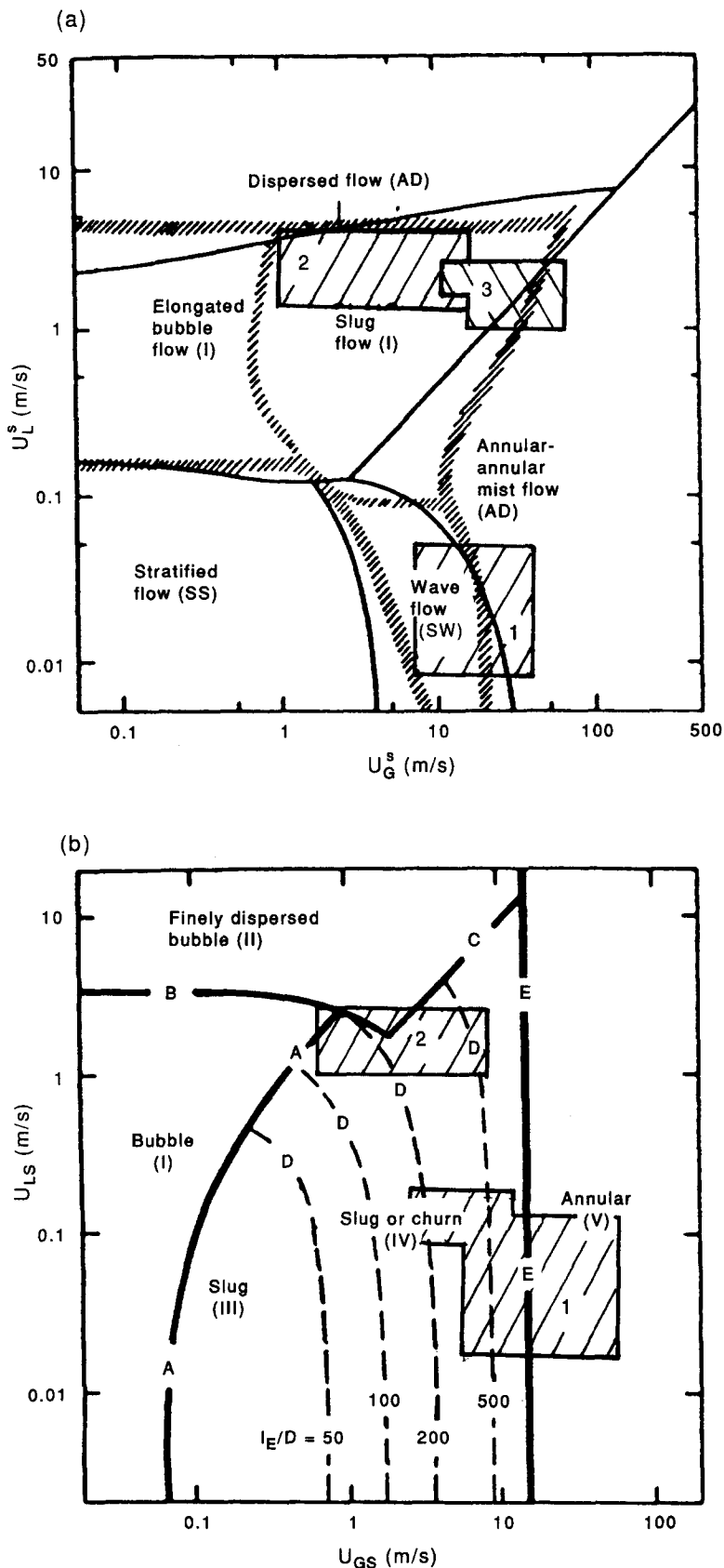


Fig. 1. Flow regimes of some of the available experimental data. Data: 1—Azzopardi *et al.* [2, 3, 5]; 2—Lahey *et al.* [4, 9, 10]; 3—Seeger *et al.* [1]. (a) Horizontal; (b) vertical.

thickness of the liquid film varies in the circumferential direction, data is reported in Refs [7, 8]. The data show that the liquid from the film is preferentially extracted at low gas take-off ratios $(Q_3/Q_1)_G < 0.3$, but progressively, more gas is extracted as that ratio increases.

Lahey and co-workers [4, 9, 10] considered higher mass fluxes, $G_1 \approx 1300\text{--}2700\text{ kg/s/m}^2$, and lower qualities, $x_1 \approx 0.1\text{--}1.0\%$ (although average void-fractions are still high with volumetric gas ratios of $\beta \approx 40\text{--}85\%$). Figure 1, which presents the Taitel and Dukler [11, 12] vertical and horizontal flow regime maps, shows that this air–water data lies mostly in the slug and non-dispersed bubbly regimes ($J_L \approx 1\text{--}3\text{ m/s}$ and $J_G \approx 1\text{--}10\text{ m/s}$). The T-junction was originally placed vertically, with the side arm in the horizontal position [9], and later horizontally [4, 10]. The collected data show that gas is preferentially extracted through the side arm, with the exception of some of the data at low Q_3/Q_1 (< 0.1) presented in Ref. [4]; for extraction ratios > 0.3 there is almost complete separation. References [4, 10] reveal that the important parameter influencing phase separation is the extraction ratio, and that the branch angle, inlet flow rate and vertical/horizontal T-configurations, have little effect.

Wider variations in inlet conditions are included in the data of Seeger *et al.* [1] (see also Ref. [13]), with $G_1 \approx 500\text{--}7000\text{ kg/s/m}^2$, $x_1 \approx 0.2\text{--}35\%$ at high pressures $p_1 \approx 4\text{--}10\text{ bar}$. Figure 1 reveals that the corresponding flow regimes are dispersed bubble, slug and annular ($J_G \approx 2\text{--}40\text{ m/s}$ and $J_L \approx 0.5\text{--}7\text{ m/s}$). However, for the bubble regime (and also for cases in the slug regime which are close to the bubble regime), there are only a few measurements and the extraction ratio was not varied in a systematic way, thus undermining the usefulness of the data for the purpose of validation for the present calculations. The side arm was oriented along three directions: vertically upwards, vertically downwards and horizontal. For the horizontal case, the data trend is as expected; gas is preferentially extracted showing a maximum of x_3/x_1 at $Q_3/Q_1 \approx 0.3$ and almost complete separation at extraction ratios > 0.5 .

Discrepancies are present in the results of the above-mentioned works, as revealed in Fig. 2, which shows data for approximately the same superficial velocities ($J_G = 5\text{ m/s}$, $J_L = 2\text{ m/s}$, slug flow, $G_1 \approx 2000\text{ kg/s/m}^2$): the data of Hwang *et al.* [4] shows a much higher degree of separation than those of Seeger *et al.* [1].

More recently, additional experimental works have emerged focusing mainly on the annular regime in horizontal T-junctions. Ballyk *et al.* [14] measured phase separation and pressure drop in low-quality, high mass-flux steam–water flows, showing that total gas separation occurs for $W_3/W_1 > 0.3$ and that $(x_3/x_1)_{\max}$ increases when the quality decreases. Rubel *et al.* [15] did the same for high-quality, low mass fluxes, encompassing the wavy and wavy/annular transition flows, showing that the effect of flow regime is more important than G_1 or x_1 .

Experimental works which report local quantities are those of Popp and Sallet [16], who measured liquid velocities with LDA in low void-fraction bubbly flows, Davis and Fungtamasan [17], who reported void-fraction profiles in churn-turbulent flows, and McCreery and Banerjee [18], who measured outlet velocity profiles for droplet flow.

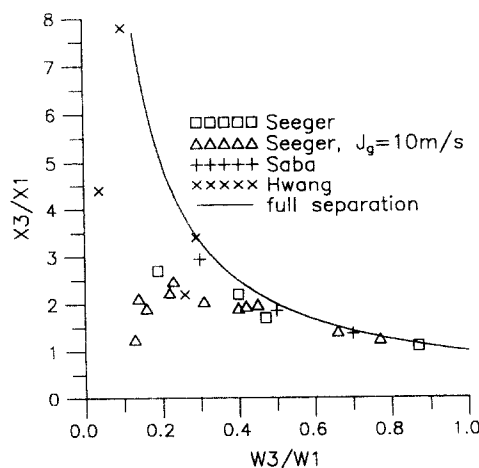


Fig. 2. Phase separation data for $J_G = 5\text{ m/s}$ and $J_L = 2\text{ m/s}$.

Table 1. Experimental work on two-phase flow in dividing T-junctions (chronological order)

| Author(s) | Position | | Fluids | D_1 [mm] | D_3/D_1 [mm] | G_1 [kg/s/m ²] | x_1 [%] | W_3/W_1 | p_1 [b] | Regime | Fluid extracted |
|---------------------------------|----------|------|--------|---------------|-------------------|---------------------------------|--------------|---------------|--------------|----------|--------------------|
| | Main | Arm | | | | | | | | | |
| Fouda and Rhodes [19] | H | V | A/W | 51 | 0.5 | 90–170 | 35–60 | 0.3–0.8 | 1.4 | A | G |
| Collier [20] | H | H | A/W | 38 | 0.66 | 140 | 2.1–50 | 0.3–0.5 | 2 | A | G |
| Hong [21] | H | H, V | A/W | 9.5 | 1.0 | 15–80 | 25–97 | 0–1 | 1.5 | W, A | L |
| Henry [22] | H | H | A/W | 100 | 0.2 | 200–850 | 10–60 | <0.06 | 1 | A | G |
| Whalley and Azzopardi [23] | V, H | H | A/W | 32 | 0.4 | 80–160 | 10–80 | <0.2 | 1.5 | A | G, L |
| Azzopardi and Baker [24] | V | H | A/W | 32 | 0.4 | 80–160 | 10–80 | <0.2 | 1.5 | C | L |
| Honan and Lahey [9] | V | H | A/W | 38 | 1.0 | 1355–2700 | <1 | 0.3, 0.5, 0.7 | 1.5 | SI | G |
| Popp and Sallet [16] | V | H | A/W | 25 × 100 | 1.0 | 1500 | 0.003 | 0.36, 0.7 | 1 | B | G |
| Azzopardi and Freeman-Bell [25] | V | H | A/W | 32 | 0.8, 1 | 80–160 | 10–80 | <0.2 | 1.5 | A | G |
| Saba and Lahey [10] | H | H | A/W | 38 | 1.0 | 1355–2700 | <1 | 0.3, 0.5, 0.7 | 1.5 | SI | G |
| Seeger <i>et al.</i> [1] | H | H, V | A, S/W | 50 | 1.0 | 500–7000 | <1 | 0–1 | 6–100 | SI, B, A | G |
| Azzopardi and Purvis [3] | V | H | A/W | 32 | 1.0 | 80–170 | 2–90 | 0–1 | 1.5 | A, C | G, L |
| Hwang <i>et al.</i> [4] | H | H | A/W | 38 | 1.0 | 1355–2700 | <1 | 0–1 | 1.5 | SI | G |
| Rubel <i>et al.</i> [15] | H | H | S/W | 38 | 1.0 | 15–50 | 20–87 | 0.2–0.8 | 1–2 | SI, W | G, L |
| Ballyk [14] | H | H | S/W | 26 | 1.0 | 450–1200 | 2–15 | 0–1 | <2.5 | A | G |
| Azzopardi and Memory [7] | H | H | A/W | 38 | 0.7–1 | 30–150 | 17–90 | 0–1 | 3 | A, W | G, L |
| Azzopardi and Smith [8] | H | H, V | A/W | 38 | 0.3–1 | 77–144 | 28–90 | 0–1 | 1.5, 3 | A, W | G, L |
| McCreery and Banerjee [18] | H | H | W/A | 25 × 75 | 1.0 | 20–60 | ≈99 | Few | 1 | D | G |
| Davis and Fungtamasan [17] | V | H | A/W | 50 | 0.5, 1 | 3000–7000 | 0.25 | 0.1–0.6 | 2.5 | B, C | G |

Regimes: A—annular; B—bubbly; C—churn; S—stratified; SI—slug; W—wavy; SA—semi-annular; D—droplet.

Fluids: A—air; W—water; S—steam.

Position: H—horizontal; V—vertical; u—upwards; d—downwards;

Last column: fluid preferentially extracted, G—gas; L—liquid.

The published experimental research on two-phase flow through T-junctions is summarized in Table 1.

Local data, like those reported by Popp and Sallet [16], serve to assess the predicted two- and three-dimensional flow fields. Unfortunately the work does not report phase separation data together with local measurements; hence those have to be taken from other studies [e.g. 1, 4] where measurements are taken in the finely dispersed flow regime. However, as shown in Table 1, most studies are in the annular regime, and so the range of data sets for comparison is somewhat limited.

THE MODEL

The method solves the full three-dimensional, two-fluid model transport equations (composed of six momentum and two continuity equations), whereby both phases are treated as interpenetrating dispersed continua in a Eulerian frame [26]. Turbulence is catered for by the use of an ensemble-averaged form of the transport equations; thus all quantities appearing in the equations below, such as the velocity U_i , refer to ensemble-averaged variables (see the turbulence model below). The equations are:

Continuity,

$$(\alpha_c)_{,i} + (\alpha_c U_{c,i})_{,i} = 0 \quad (1)$$

and

$$(\alpha_d)_{,i} + (\alpha_d U_{d,i})_{,i} = 0; \quad (2)$$

momentum,

$$\begin{aligned} (\alpha_c \rho_c U_{c,i})_{,i} + (\alpha_c \rho_c U_{c,i} U_{c,j})_{,j} = & -\alpha_c p_{,i} + (\alpha_c \mu_c^{\text{ef}} (U_{c,i,j} + U_{c,j,i} - \frac{2}{3} U_{c,k,k} \delta_{ij}))_{,i} \\ & + \alpha_d \rho_d A_D (U_{d,i} - U_{c,i}) + g_i \alpha_c \rho_c + S_{u_{c,i}} \end{aligned} \quad (3)$$

and

$$\begin{aligned} (\alpha_d \rho_d U_{d,i})_{,i} + (\alpha_d \rho_d U_{d,i} U_{d,j})_{,j} = & -\alpha_d p_{,i} + (\alpha_d \mu_d^{\text{ef}} (U_{d,i,j} + U_{d,j,i} - \frac{2}{3} U_{d,k,k} \delta_{ij}))_{,i} \\ & + \alpha_d \rho_d A_D (U_{c,i} - U_{d,i}) + g_i \alpha_d \rho_d + S_{u_{d,i}}; \end{aligned} \quad (4)$$

and

compatibility,

$$\alpha_c = 1 - \alpha_d. \quad (5)$$

In the above equations, α stands for the phase volume-fraction and the subscripts c and d stand for the continuous (liquid, L) and dispersed phases (gas, G) respectively. The effective viscosity is the sum of the molecular and turbulent contribution, $\mu^{\text{ef}} = \mu + \mu^t$, with $\mu^t = \rho \nu^t$ to be obtained from the turbulence model. Although our interest is in the steady state only, the time dependent terms are included because they are used in the numerical method in which marching in time is effected until a steady state is reached. The term containing A_D represents interphase momentum transfer which is assumed for the present calculations to arise from drag alone in the absence of high accelerations. The assumption that forces other than drag are negligible compared with the drag has been confirmed by *a posteriori* analysis of the resulting relative velocity fields, where it was found other forces such as virtual mass are at least an order of magnitude smaller than the drag force.

As the application considered relates to bubbly flow, the drag is computed using a drag coefficient (C_D) derived from the assumption that the bubbles are spherical particles of uniform radius. To allow for high gas phase fractions ($\alpha \equiv \alpha_d$) the drag coefficient is modified by an empirical correction factor, $f(\alpha)$. Thus:

$$A_D = 3/4(\rho_c V_r C_D)/(\rho_d d_b), \quad (6)$$

and

$$C_D = (24/\text{Re}_b)(1 + 0.15\text{Re}_b^{0.687}) \cdot f(\alpha), \quad (7)$$

where V_r is the modulus of the slip velocity, Re_b is the bubble Reynolds number and d_b is the bubble diameter. C_D and the function $f(\alpha)$ are obtained from Zuber [27]; two forms for the expression $f(\alpha)$

have been considered: $1/(1 - \alpha)^2$ which accounts for the effect of α on the drag, and $(1 - \alpha)$ which recovers the right limit of zero drag as $\alpha \rightarrow 1$. The sensitivity of the results to these expressions is outlined later.

The source terms, S_u , arise from the extension of the turbulence model to two phase flow and are discussed below.

Turbulence Model

Two turbulence models have been implemented; both are variants of the well-established $k-\epsilon$ model. In both, turbulence is assumed to be generated within the continuous (liquid in this case) phase only. Thus, the phase fraction α_c now features in the transport equations for k and ϵ (see below).

In the first model employed, the phase fraction α_c was assumed not to fluctuate. Time-averaging of the governing equations (1)–(5), (18) and (19) does not in this case yield any new terms additional to those obtained in averaging the single-phase equations. Thus, terms $S_{u_{c_i}}$ and $S_{u_{d_i}}$ in equations (3) and (4) are both zero.

In the second model, the instantaneous phase fraction (denoted by $\hat{\alpha}$) is taken to fluctuate as was done by Gosman *et al.* [28]. Hence:

$$\hat{\alpha} = \alpha + \alpha', \quad (8)$$

where α is the ensemble-averaged value and α' is the fluctuation component. All terms in the instantaneous governing equations are then ensemble-averaged using the Favre weighting, with $\hat{\alpha}$ being the weighting factor (each phase is weighted by its own phase fraction). Thus, if the instantaneous velocity is u_i and the fluctuation component is u_i'' , then:

$$u_i = U_i + u_i''. \quad (9)$$

Favre-averaging assumes that the ensemble-averaging of the product ($\hat{\alpha}u_i''$) vanishes. Hence, from equations (8) and (9):

$$\begin{aligned} \overline{\hat{\alpha}u_i} &= \overline{\hat{\alpha}(U_i + u_i'')} \\ &= \alpha U_i. \end{aligned}$$

Hence:

$$U_i = \frac{\overline{\hat{\alpha}u_i}}{\alpha}. \quad (10)$$

Thus, U_i appearing in the governing equations is the α -weighted ensemble-average of u_i . Full details of this averaging process are found in the work of Politis [29].

As an outcome of this averaging procedure, additional terms arise in the equations. One of the more important of these in the momentum equations results from the averaging of the instantaneous drag term:

$$f_{D_d} = A_D \rho_d \cdot \hat{\alpha}_d (u_{c_i} - u_{d_i}), \quad (11)$$

which when averaged leads to

$$\begin{aligned} \overline{\hat{\alpha}_d u_{c_i}''} &= \overline{(1 - \hat{\alpha}_c) u_{c_i}''} \\ &= \overline{u_{c_i}''} - \overline{\hat{\alpha}_c u_{c_i}''} \\ &= u_{c_i}'' \quad (\text{since } \overline{\hat{\alpha}_c u_{c_i}''} = 0 \text{ by definition}). \end{aligned}$$

The term $\overline{u_{c_i}''}$ is now modelled, as is the case with all other terms arising from the Favre-averaging, using the eddy-diffusivity concept as

$$\overline{u_{c_i}''} = -\frac{\nu^t}{\sigma_x \alpha_c} (\alpha_d)_{,i}. \quad (12)$$

The other extra terms in the momentum equations arise from the modelling of the continuous phase turbulent stresses, which after the usual assumption based on the eddy diffusivity [29] take the form

$$-\overline{\alpha_c u_{c_i}'' u_{c_j}''} = -\frac{2}{3} \alpha_c k \delta_{ij} + \alpha_c \nu^t (U_{c_{i,j}} + U_{c_{j,i}}) - \frac{2}{3} \alpha_c \nu^t U_{c_{i,l}} \delta_{ij}. \quad (13)$$

For the dispersed phase a similar expression can be obtained. However to enable this, a relationship between the fluctuation components u''_{c_i} and u''_{d_i} is needed. This is postulated to be given by

$$C_i \equiv \frac{u'_d}{u'_c}, \quad (14)$$

where C_i is a measure of the response time of an individual bubble to the fluctuating velocity of the liquid. A simplified analysis [28] of the motion of a single bubble gives the following expression for C_i .

$$C_i = 1 - \exp(-t_i/t_p), \quad (15)$$

where the eddy lifetime t_i is calculated as $0.4k/\epsilon$, and the particle (in this case bubble) relaxation time t_p is taken as $(1/A_D)(1 + 0.5\rho_c/\rho_d)$.

From equations (12) and (13), the source terms S_{u_c} and S_{u_d} in the momentum equations become

$$S_{u_{c_i}} = -2/3(\rho_c \alpha_c k)_{,i} + (A_D \rho_d \rho_c v^1)/(\sigma_z \alpha_c \rho_c)(\alpha_{d,i}) \quad (16)$$

and

$$S_{u_{d_i}} = -2/3(\rho_d \alpha_d C_i^2 k)_{,i} - (A_D \rho_d \rho_c v^1)/(\sigma_z \alpha_c \rho_c)(\alpha_{d,i}). \quad (17)$$

The turbulent eddy diffusivity is given by $v^1 = C_\mu k^2/\epsilon$, where the turbulence kinetic energy k and its rate of dissipation ϵ are determined from transport equations pertaining to the k - ϵ model. These equations now account for the presence of two phases and take the form [28]:

$$(\alpha_c \rho_c k)_{,i} + (\alpha_c \rho_c U_{c_j} k)_{,j} = (\alpha_c (\mu_c^{\text{ef}}/\sigma_k) k_{,j})_{,j} + G - \rho_c \alpha_c \epsilon + S_k \quad (18)$$

and

$$(\alpha_c \rho_c \epsilon)_{,i} + (\alpha_c \rho_c U_{c_j} \epsilon)_{,j} = (\alpha_c (\mu_c^{\text{ef}}/\sigma_\epsilon) \epsilon_{,j})_{,j} + \epsilon/k (C_1 G - C_2 \rho_c \alpha_c \epsilon) + S_\epsilon, \quad (19)$$

where S_k and S_ϵ are additional source terms arising from fluctuations of α when these are accounted for. They are given by

$$S_k = -2A_D(1 - C_i)\rho_d \alpha_d k - (A_D \rho_d v^1)/(\sigma_z \alpha_c)(U_{d_i} - U_{c_i})\alpha_{d,i} \quad (20)$$

and

$$S_\epsilon = -2A_D(1 - C_i)\rho_d \alpha_d \epsilon. \quad (21)$$

Both terms in equation (20) originate from the ensemble-averaging of the drag force when the k equation is derived from the continuous phase equations. The first term in equation (20) arises from the correlation $\hat{\alpha}_d u''_{c_i}(u''_{d_i} - u''_{c_i})$ and the second from $\hat{\alpha}_d u''_{c_i} \cdot (U_{d_i} - U_{c_i})$, which is modelled as in equation (12). The source for the ϵ equation is derived by Gosman *et al.* [28] and represents an additional source of dissipation rate, due to the bubble response lag. The effective viscosity of the dispersed phase in equation (4) is obtained from $\mu_d^{\text{ef}} = \mu_d + \rho_d C_i^2 v^1$, where use has been made of equation (14).

It should be noted that, if the additional sources represented by equations (16), (17), (20) and (21) are set to zero, the unmodified k - ϵ model (where the α fluctuations are ignored) is recovered; that model assumes that the turbulence of the continuous phase is not affected by the presence of bubbles.

Values of all the constants in the turbulence model used are the same as those recommended for the single-phase flow model [30].

NUMERICAL METHOD

The governing equations are solved numerically using a finite-volume technique with all variables stored at cell centres on the mesh [31]. The spatial differencing scheme is simple upwind for the convection terms and centered for the diffusion terms. A special addressing scheme was implemented to efficiently handle the partially unstructured mesh employed to discretize the multiply-connected domain of the T-junction geometry. With this "indirect-addressing" no computational cells are wasted outside of the T-junction to mesh the enveloping rectangular domain, as would happen with standard procedures [e.g. 32].

The discretized set of equations is solved iteratively and sequentially using an adaptation of the SIMPLE method [33] for single-phase flows, suitably extended to cater for two phases. Here the pressure correction is based on the sum of the two continuity equations, each normalized by a reference phase density (as in Ref. [34]). The phase fraction field is determined by solving the dispersed phase continuity equation as a transport equation in terms of α_d .

In what follows the discretization of the transport equations and the algorithm for solving the resulting set of discretized equations are outlined.

General Form of the Equations

The methodology developed is general in the sense that non-orthogonal computational meshes are allowed for, so that domains of irregular shapes can be overlaid with meshes that conform to the boundaries. This will be especially useful for further applications to T-junctions formed with circular cross-section pipes; for the present case, however, the non-orthogonal mesh capability, although built in, is not exercised. As a starting point for the generalization, equations (1)–(4) have to be recast in a form in which the independent variables are general coordinates (ξ_l , $l = 1, 2, 3$ for ξ, η, ζ). The velocities, however, are still taken to be aligned along a Cartesian coordinate frame. In recasting the equations, the derivatives are transformed according to

$$\begin{aligned}(\cdot)_{,l} &\rightarrow (J \cdot)_{,l}/J, \\ (\cdot)_{,j} &\rightarrow (\beta_{lj} \cdot)_{,l}/J,\end{aligned}\quad (22)$$

where J is the Jacobian of the transformation (x_l) \rightarrow (ξ_l) and β_{lj} are metric quantities defined as the components of the vector $\beta_l = \mathbf{x}_{,l+1} \times \mathbf{x}_{,l+2}$ (l cyclic). After application of these transformation rules the equations become:

$$\begin{aligned}(\alpha \rho J)_{,l} + (\rho \beta_{lj} \alpha U_j)_{,l} &= 0, \\ (J \alpha \rho U_i)_{,l} + (\rho \beta_{lj} \alpha U_i U_j)_{,l} &= -\alpha \beta_{li} (p)_{,l} + (\alpha \beta_{lj} \tau_{ij})_{,l} + J \rho \alpha g_i + J S_{u_i} + J \alpha_d \rho_d A_D V_{r_i}, \\ \tau_{ij} &= \frac{\mu^{\text{ef}}}{J} ((\beta_{nj} U_i)_{,n} + (\beta_{mi} U_j)_{,m}) - \frac{2\mu^{\text{ef}}}{3J} (\beta_{nk} U_k)_{,n} \delta_{ij}.\end{aligned}\quad (23)$$

Equations (23) apply for each of the two phases in which U is the velocity of the phase in question (and may take either subscript c or d) and V_r is the slip velocity between the phases. The equations for k and ϵ , similarly transformed become:

$$\begin{aligned}(J \alpha_c \rho_c k)_{,l} + (\rho_c \beta_{lj} \alpha_c U_{c_j} k)_{,l} &= \left(\alpha_c \beta_{lj} \frac{\mu_c^{\text{ef}}}{J} (\beta_{nj} k)_{,n} \right)_{,l} + J(G - \rho_c \alpha_c \epsilon) + J S_k, \\ (J \alpha_c \rho_c \epsilon)_{,l} + (\rho_c \beta_{lj} \alpha_c U_{c_j} \epsilon)_{,l} &= \left(\alpha_c \beta_{lj} \frac{\mu_c^{\text{ef}}}{J} (\beta_{nj} \epsilon)_{,n} \right)_{,l} + \frac{\epsilon}{k} J (C_1 G - C_2 \rho_c \alpha_c \epsilon) + J S_\epsilon.\end{aligned}\quad (24)$$

Discretization

The equations above are integrated following the work of Peric [35] over a general six-sided control volume, of which a two-dimensional representation is shown in Fig. 3. In this process the

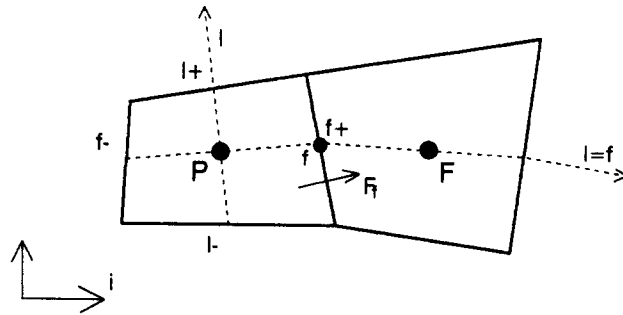


Fig. 3. Sketch of the general control volume (cell) and directions.

geometrical quantities J and β , become \mathcal{V} (cell volume) and B_{ij} (j -component of area of cell face along direction i). The derivatives of a general variable ϕ , denoted by $(\phi)_{,l}$, become simple differences of neighbour values along direction l , thus:

$$\begin{aligned} [\Delta\phi]_l^p &= \phi^{l+} - \phi^{l-}, \\ [\Delta\phi]_{f=f}^f &= [\Delta\phi]_{f=f}^f = \phi^F - \phi^P, \end{aligned} \quad (25)$$

where F and P superscripts denote center-of-cell values and f and l denote values at cell faces (Fig. 3). For the convective terms, standard upwind differences are used. With these rules the integration of each term in the equations above leads to:

$$(J\alpha\rho U_i)_{,t} \rightarrow \left(\frac{\mathcal{V}\alpha\rho U_i}{\delta t} \right)^P - \left(\frac{\mathcal{V}\alpha\rho U_i^n}{\delta t} \right)^P, \quad (26)$$

$$(\rho\beta_{ij}\alpha U_i U_j)_{,l} \rightarrow \sum_{l=1}^3 [\Delta(F_l U_i)]_{l_{\text{upwind}}} = \sum_{f=1}^6 F_{f_{\text{upwind}}} [\Delta U_i]_f^f, \quad (27)$$

$$\alpha\beta_{ii}(p)_{,l} \rightarrow \alpha^P \sum_{l=1}^3 B_{ii}^P [\Delta p]_l^P, \quad (28)$$

$$\begin{aligned} (\alpha\beta_{ij}\tau_{ij})_{,l} &\rightarrow \sum_{l=1}^3 \left[\Delta \left(\alpha \sum_j B_{ij}\tau_{ij} \right) \right]_l \\ &= \sum_{f=1}^6 (-1)^f \left(\frac{\alpha\mu}{\mathcal{V}} \right)^f \left(\sum_j \sum_m \beta_{ij}^f B_{mj}^f [\Delta U_i]_m^f + \sum_j \sum_m B_{ji}^f B_{mi}^f [\Delta u_j]_m^f \right) - \frac{2}{3} \frac{\alpha\mu}{\mathcal{V}} \sum_l B_{ii}^P [\Delta F]_l \end{aligned} \quad (29)$$

and

$$(J\rho\alpha g_i) \rightarrow (\mathcal{V}\rho\alpha g_i)^P, \quad (30)$$

where implicit differencing in time is assumed, and all variables are taken to be at the new time level t^{n+1} , except those with superscript n which denote old time level values. Quantities F_f represent convective fluxes at face f , the definition of which is given later. The convective terms are upwinded, which is equivalent to defining

$$\begin{aligned} F_{f_{\text{upwind}}} &= \max(F_f, 0) \quad \text{for } f = f^- \\ &= \min(F_f, 0) \quad \text{for } f = f^+. \end{aligned} \quad (31)$$

In the expressions above, quantities which are not stored at cell faces are computed by means of the arithmetic average, $\bar{\phi}^f = (\phi_P + \phi_F)/2$.

Discretized Equations

The equations are cast in the general form (for any variable ϕ):

$$A_P \phi_P = \sum_{f=1}^6 A_f \phi_f + S, \quad (32)$$

where S is the source term and the A s are coefficients defined as follows:

$$\begin{aligned} A_f &= D_f + |F_{f_{\text{upwind}}}| = D_f + \max(F_f, 0) \quad \text{for } f = f^- \\ &= D_f - \min(F_f, 0) \quad \text{for } f = f^+, \end{aligned} \quad (33)$$

with the diffusion flux defined by

$$D_f = \left(\frac{\alpha\mu}{\mathcal{V}} \right)^f \sum_j B_{ji}^f B_{ji}^f = \frac{(\alpha\mu)^f}{\mathcal{V}_f} B_f^2, \quad (34)$$

where

$$\mathcal{V}_f \equiv [\Delta \mathbf{x}]_f^f \cdot \mathbf{B}_f = \sum_j [\Delta x_j]_f^f B_{ji}^f.$$

Hereafter the contribution of surrounding cells will be denoted as $H(\phi) \equiv \sum_f A_f \phi_f$, with $A_0 \equiv \sum_f A_f$. The individual discretized equations for the different variables are therefore:

continuous phase momentum,

$$\left(A_0^c + \frac{\alpha_c \rho_c \mathcal{V}}{\delta t} \right) U_{c_i} = H_c^n(U_{c_i}) - \alpha_c^p \sum_l^3 B_{li}^p [\Delta p]_l^p + F_D(U_{d_i} - U_{c_i}) + S_{u_i}^c + \frac{\alpha_c \rho_c \mathcal{V}}{\delta t} U_{c_i}^n, \quad (35)$$

where $F_D \equiv \mathcal{V} \alpha_d \rho_d A_D$ and the term $S_{u_i}^c$ contains the cross-derivative terms arising from the transformation of the stress terms into non-orthogonal coordinates;

dispersed phase momentum,

$$\left(A_0^d + \frac{\alpha_d \rho_d \mathcal{V}}{\delta t} \right) U_{d_i} = H_d^n(U_{d_i}) - \alpha_d^p \sum_l^3 B_{li}^p [\Delta p]_l^p + F_D(U_{c_i} - U_{d_i}) + S_{u_i}^d + \frac{\alpha_d \rho_d \mathcal{V}}{\delta t} U_{d_i}^n, \quad (36)$$

here also $S_{u_i}^d$ contains similar terms to those in $S_{u_i}^c$;

continuous phase continuity,

$$\frac{\rho_c \mathcal{V}}{\delta t} (\alpha_c - \alpha_c^n) + \sum_f^6 (-1)^f F_{f_c} = 0; \quad (37)$$

and

dispersed phase continuity,

$$\frac{\rho_d \mathcal{V}}{\delta t} (\alpha_d - \alpha_d^n) + \sum_f^6 (-1)^f F_{f_d} = 0. \quad (38)$$

The fluxes F_f are defined as

$$F_f \equiv \tilde{\alpha}^f \rho \sum_j B_{fj}^f \tilde{U}_j^f, \quad (39)$$

where $\tilde{\alpha}^f$ denotes an upwinded volume-fraction at point f , obtained from either α_p or α_f (Fig. 3) according to the sign of $F_f' \equiv \rho \sum_j B_{fj}^f \tilde{U}_j^f$. The “face velocities” \tilde{U} are velocities interpolated at cell faces using a special interpolation practice (introduced by Rhie and Chow [31]) so that pressure decoupling on the non-staggered mesh is avoided. The formulation given here avoids another problem, which is that of the dependence of steady-state solution on the time step [36, 37]. Thus,

$$\tilde{U}_i^f = \left(\overline{A_p^u U_i^f} + \overline{\alpha^p B_{fi}^p [\Delta p]_f^p} - \tilde{\alpha}^f B_{fi}^f [\Delta p]_f^f + \left(\frac{\alpha \rho \mathcal{V}}{\delta t} \right)^f \tilde{U}_i^n - \left(\frac{\alpha \rho \mathcal{V}}{\delta t} U_i^n \right)^f \right) / \overline{A_p^u}^f \quad (40)$$

where A_p is the central coefficient defined in equation (32). By substitution in the flux equation (39), the expression actually used in the computations becomes:

$$F_f = \frac{1}{\overline{A_p^u}^f} \left\{ \left(\frac{\alpha \rho \mathcal{V}}{\delta t} \right)^f F_f^n + \tilde{\alpha}^f \rho \sum_i^3 B_{fi}^f \left(\overline{A_p^u U_i} + \overline{\alpha^p B_{fi}^p [\Delta p]_f^p} - \left(\frac{\alpha \rho \mathcal{V}}{\delta t} U_i^n \right)^f - \tilde{\alpha}^f B_{fi}^f [\Delta p]_f^f \right) \right\}. \quad (41)$$

This expression is free from δt dependency, since in the limit of the converged (or steady-state) solution $F_f^n \rightarrow F_f$ and $u_i^n \rightarrow u_i$, and terms involving δt cancel out (noting that $A_p = A_0 + \alpha \rho \mathcal{V} / \delta t$).

Sum of dispersed and continuous phase continuities

$$\left\{ \frac{\mathcal{V}}{\delta t} (\alpha_c - \alpha_c^n) + \sum_f^6 (-1)^f F_{f_c} / \rho_c \right\} + \left\{ \frac{\mathcal{V}}{\delta t} (\alpha_d - \alpha_d^n) + \sum_f^6 (-1)^f F_{f_d} / \rho_d \right\} = 0,$$

and since $\alpha_d + \alpha_c = \alpha_d^n + \alpha_c^n = 1$, the time-derivative terms vanish. Hence,

$$\sum_f^6 (-1)^f (F_{f_c} / \rho_c + F_{f_d} / \rho_d) = 0. \quad (42)$$

Dispersed phase continuity as an α equation (here $\alpha = \alpha_d$)

$$\left(A_0^\alpha + \frac{\rho_d \mathcal{V}}{\delta t} + \max[\text{div}(U_d), 0] \right) \alpha = H_\alpha^n(\alpha) + \max[-\text{div}(U_d), 0] + \frac{\rho_d \mathcal{V}}{\delta t} \alpha^n, \quad (43)$$

where the coefficients are made up of convective fluxes only, and

$$\begin{aligned} A_f^\alpha &= \max(F'_{fd}, 0) \quad \text{for } f = f^- \\ A_f^\alpha &= -\min(F'_{fd}, 0) \quad \text{for } f = f^+; \end{aligned} \quad (44)$$

F' is a flux without volume-fraction

$$\text{(i.e. } F' = F/\tilde{\alpha}) \quad \text{and} \quad \text{div}(U_d) = \sum_f^6 (-1)^f F'_{fd}.$$

Turbulent kinetic energy

$$\left(A_0^k + \frac{\alpha_c \rho_c \mathcal{V}}{\delta t} \right) k = H_k^n(k) + S^k + \mathcal{V}(G - \rho_c \alpha_c \epsilon) + \frac{\alpha_c \rho_c \mathcal{V}}{\delta t} k^n. \quad (45)$$

Here S^k contains the cross-derivative terms arising from the non-orthogonal coordinates.

Turbulent dissipation

$$\left(A_0^\epsilon + \frac{\alpha_c \rho_c \mathcal{V}}{\delta t} \right) \epsilon = H_\epsilon^n(\epsilon) + S^\epsilon + \mathcal{V} \frac{\epsilon}{k} (C_1 G - C_2 \rho_c \alpha_c \epsilon) + \frac{\alpha_c \rho_c \mathcal{V}}{\delta t} \epsilon^n, \quad (46)$$

with S^ϵ containing the cross-derivative terms.

The Solution Algorithm

The above sets of discretized equations are solved iteratively in a sequential manner whereby the velocity, pressure and scalars at a new time (or iteration) level (" $n + 1$ ") are computed from their value at the previous time (or iteration) level (" n "). This advancement in time is used herein as a pseudo time-marching technique and may not be time accurate. The algorithm falls in the fully-implicit class, with the pressure being obtained from a pressure-correction equation derived from a combination of the continuity and momentum equations—see the Appendix. The explanation of the algorithm given below adopts the splitting concept and terminology introduced by Issa [38]. The steps in the algorithm are as follows:

1. Solve the continuous phase momentum equation:

$$\begin{aligned} \left(A_0^c + \frac{\alpha_c \rho_c \mathcal{V}}{\delta t} \right) U_{ci}^* &= H_c^n(U_{ci}^*) - \alpha_c^p \sum_l^3 B_{li}^p [\Delta p^n]_l^p \\ &+ F_D(U_{di}^n - U_{ci}^n) + S_{ui}^c + \frac{\alpha_c \rho_c \mathcal{V}}{\delta t} U_{ci}^n, \end{aligned} \quad (47)$$

where the superscript $*$ denotes intermediate values.

2. Solve the dispersed phase momentum equation:

$$\begin{aligned} \left(A_0^d + \frac{\alpha_d \rho_d \mathcal{V}}{\delta t} + F_D \right) U_{di}^* &= H_d^n(U_{di}^*) - \alpha_d^p \sum_l^3 B_{li}^p [\Delta p^n]_l^p \\ &+ F_D U_{ci}^* + S_{ui}^d + \frac{\alpha_d \rho_d \mathcal{V}}{\delta t} U_{di}^n. \end{aligned} \quad (48)$$

3. Assemble the pressure correction p' equation. The pressure and velocities are updated according to the equations formulated in the Appendix. These are:

$$A_{pp}^p p'_p = \sum_i A_{pi}^p p'_i + S_u^p, \quad (49)$$

$$\frac{\alpha_c \rho_c \mathcal{V}}{\delta t} (U_{ci}^{n+1} - U_{ci}^*) = -\alpha_c^p \sum_l^3 B_{li}^p [\Delta p^n]_l^p, \quad (50)$$

$$\left(\frac{\alpha_d \rho_d \mathcal{V}}{\delta t} + F_D \right) (U_{d_i}^{n+1} - U_{d_i}^*) = -\alpha_d^p \sum_l^3 B_l^p [\Delta p]_l^p \quad (51)$$

and

$$p^{n+1} = p^n + p'. \quad (52)$$

The fluxes F^* are corrected in the same way as the nodal velocities [equations (50) and (51)] and the corresponding expressions are (see the Appendix):

$$F_{fd}^{n+1} = F_{fd}^* - A_{fd}^p [\Delta p]_f \mathcal{V}_f \quad (53)$$

and

$$F_{fc}^{n+1} = F_{fc}^* - A_{fc}^p [\Delta p]_f \mathcal{V}_f. \quad (54)$$

- 4. Solve for all additional scalar equations.** In the present case these are the turbulence quantities to be solved for, k and ϵ :

$$\left(A_0^k + \frac{\alpha_c \rho_c \mathcal{V}}{\delta t} + \alpha_c \rho_c \mathcal{V} \frac{\epsilon^n}{k^n} \right) k^{n+1} = H_k^n(k^{n+1}) + S^k + \mathcal{V} G + \frac{\alpha_c \rho_c \mathcal{V}}{\delta t} k^n \quad (55)$$

and

$$\begin{aligned} \left(A_0^\epsilon + \frac{\alpha_c \rho_c \mathcal{V}}{\delta t} + \alpha_c \rho_c \mathcal{V} C_2 \frac{\epsilon^n}{k^{n+1}} \right) \epsilon^{n+1} &= H_\epsilon^n(\epsilon^{n+1}) + S^\epsilon \\ &+ \mathcal{V} \frac{\epsilon^n}{k^{n+1}} C_1 G + \frac{\alpha_c \rho_c \mathcal{V}}{\delta t} \epsilon^n. \end{aligned} \quad (56)$$

With new values of k and ϵ , the liquid and gas effective viscosities are updated.

- 5. The dispersed phase continuity equation.** This equation is solved implicitly in order to obtain an updated void-fraction:

$$\begin{aligned} \left(A_0^\alpha + \frac{\rho_d \mathcal{V}}{\delta t} + \max[+\operatorname{div}(U_d), 0] \right) \alpha^* &= H_\alpha^n(\alpha^*) + \max[-\operatorname{div}(U_d), 0] \\ &+ \frac{\rho_d \mathcal{V}}{\delta t} \alpha^n. \end{aligned} \quad (57)$$

The updated void-fraction and gas flux directions are used to determine upwinded cell-face void-fractions, $\tilde{\alpha}^f$, which are stored.

With this, the algorithm for two-phase flow computations is complete. The solution will be advanced in time until the normalized residuals of all the equations are smaller than a specified value (we use 10^{-4}). At this point the solution is said to be converged and, since overall continuity for the sum of the gas and liquid is satisfied together with that of the gas, continuity will also be satisfied for the liquid phase. A complete description of the method can be found in Ref. [37].

RESULTS

The experimental work of Popp and Sallet [16] is chosen here for the purpose of comparison against predictions for the following reasons: (a) local quantities were measured (velocities, using LDA); (b) the T-junction is formed from rectangular cross-sectional channels, facilitating the generation of a simple orthogonal computational mesh; (c) the incoming flow is a low void-fraction bubbly mixture ($\langle \alpha \rangle \simeq 2\%$), which is the simplest regime to model and calculate for validation purposes.

In what follows, the geometry of the flow domain and the appropriate boundary conditions are first presented, the computational meshes used are then described briefly and results obtained with different deflection ratios are given; these consist of velocity profiles in the run and branch, both for single- and two-phase flows (compared with data), and contours of void-fraction at several planes of the three-dimensional field. Comparison of phase separation ratios with the experiment is also made; however, the data used is taken from Azzopardi and Whalley [2], as Popp and Sallet

do not measure these. In the discussion of the phase segregation predictions, several parametric studies are also presented. First, calculations made with the fully extended two-phase flow turbulence model presented earlier are compared with those obtained from the simpler model which ignores phase fraction fluctuations (see the earlier section). The effect of varying the expression for interphase drag is then examined. Finally, the consequences of using different values for the bubble diameter are studied.

Geometry and Boundary Conditions

In the experiments of Popo and Sallet [16] a mixture of water and air flows through a vertical straight channel and is partially deflected at a T-junction having a side arm at 90° . All cross-sections are rectangular, having dimensions: width(W) \times depth(D) = 25×100 mm; the lengths used in the computations for the inlet, run and branch arms, are $L_1 = 5W$, $L_2 = 10W$ and $L_3 = 10W$. A complete description of the geometry and experimental apparatus can be found in the cited reference.

Inlet conditions were not given by Popp and Sallet; hence profiles corresponding to fully developed two phase flow in a channel were assumed in this work. In particular, the phase fraction distribution was taken to obey a 1/4-power formula which approximates the experimentally measured distributions reported in the literature for fully developed two-phase flow [e.g. 41].

Relevant inlet conditions are:

| | |
|--------------------------|--|
| water flow rate, | $(Q_1)_L = 1.885 \times 10^{-3} \text{ m}^3/\text{s};$ |
| gas flow rate, | $(Q_1)_G = 4.135 \times 10^{-5} \text{ m}^3/\text{s};$ |
| average void-fraction, | $\langle \alpha \rangle_1 = 2.08\%;$ |
| average liquid velocity, | $\langle U_L \rangle_1 = 1.53 \text{ m/s};$ |
| average gas velocity, | $\langle U_G \rangle_1 = 1.60 \text{ m/s};$ |
| average pressure, | $\langle p \rangle_1 = -3 \text{ N/m}^2$ |
| bubble diameter, | $d_b = 1 \text{ mm}.$ |

Boundary conditions at both outlets (run and branch) are imposed in the usual way: zero axial gradients for all variables except pressure, for which a linear extrapolation is used. At the two outlets, the total flow split between the arm and the run (Q_3 and Q_2) is determined in reality by the pressures imposed at these stations. However, since these pressures were not given in the cited

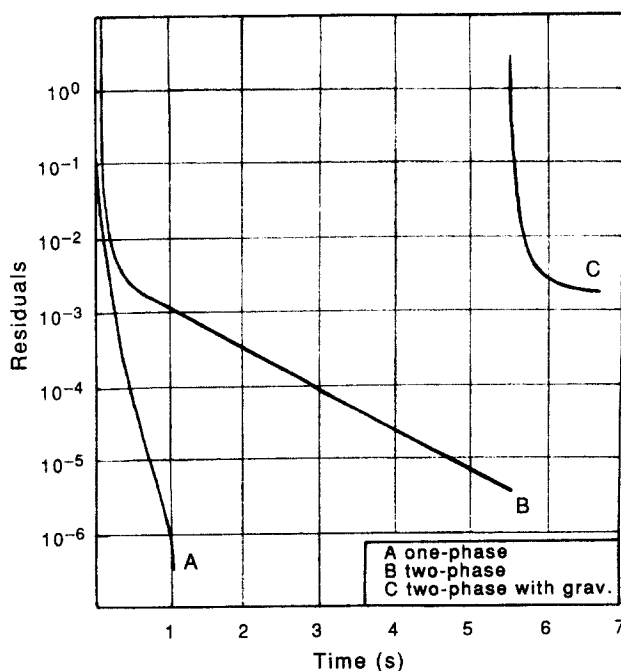


Fig. 4. Convergence history for single- and two-phase flow ($Q_3/Q_1 = 0.70$; both cases starting from zero).

reference, the measured overall flow split Q_3/Q_2 was specified instead. This still leaves the individual phase flow split to be predicted as an outcome of the solution.

Mesh Refinement and Convergence Rates

The computations were made using non-uniform finite-volume meshes. For the three-dimensional calculations, meshes with 6500 and 52,000 internal cells were used. For the two-phase flow predictions, a study of mesh refinement was made using two-dimensional configurations employing 650 and 2600 cells [the same mesh as in each (x, y) -plane of the three-dimensional configurations, with 10 and 20 cells along the z -direction, respectively]. The results pertaining to phase separation are given in Table 2.

Table 2 shows that the coarse mesh gives approximately the same value of $(Q_3/Q_1)_G$ as the fine one; it is therefore reasonable to assume that the coarse mesh calculations used for the three-dimensional computations are as accurate as their two-dimensional counterparts. The fine mesh was especially necessary for single-phase flow in order to obtain better resolution in the

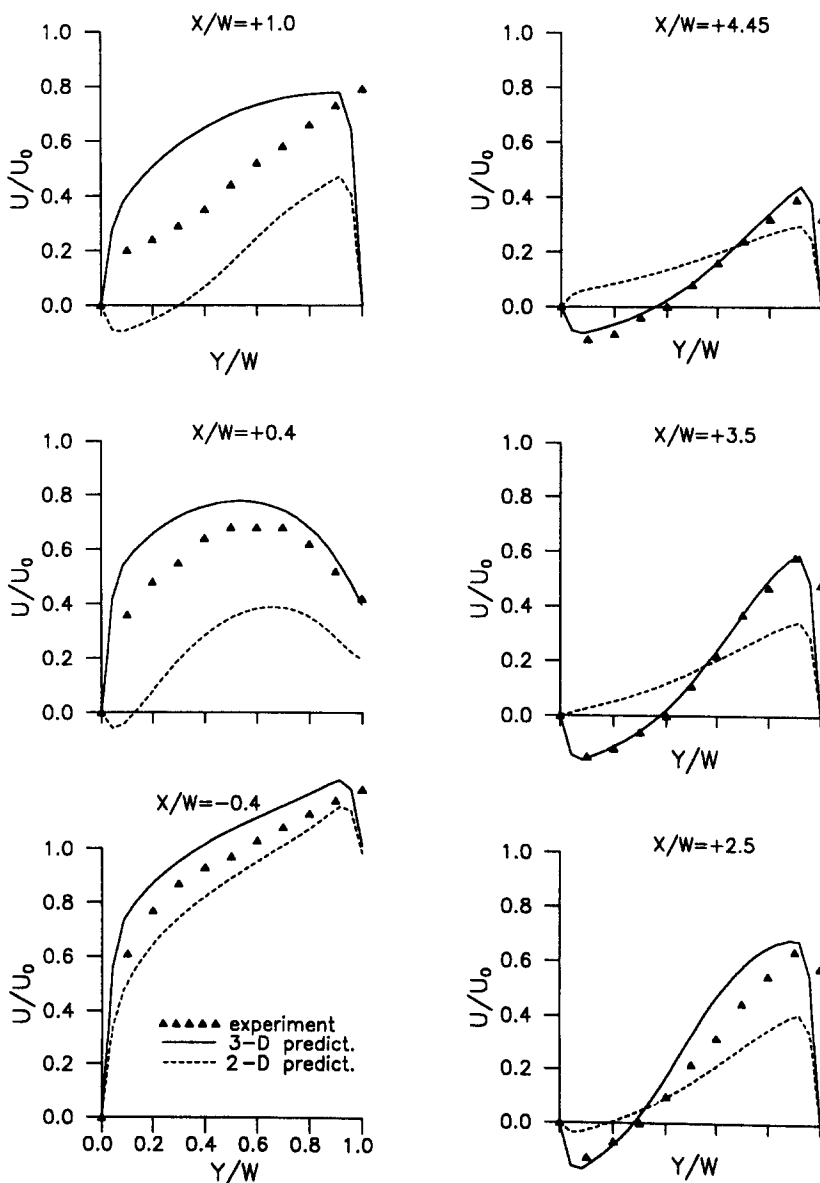


Fig. 5(a)—caption overleaf.

| Table 2. Effect of mesh refinement | | | |
|------------------------------------|-----------|---------------|--------------------------------|
| Mesh | Q_3/Q_1 | $(Q_3/Q_1)_G$ | $\langle \alpha \rangle_3$ [%] |
| Coarse | 0.70 | 0.92 | 3.4 |
| Fine | 0.70 | 0.93 | 4.2 |
| Coarse | 0.38 | 0.60 | 4.2 |
| Fine | 0.38 | 0.61 | 4.8 |

run upstream of the junction, for high deflection ratios. For these conditions the flow becomes appreciably three-dimensional, a fact also observed by Popp and Sallet; better agreement with the measurements of local water velocities could only be achieved with that fine three-dimensional mesh. Otherwise single-phase flow predictions on the coarser mesh are satisfactory, even when comparing local quantities such as velocities and pressures (discrepancies between the two meshes were around 3–8% for the axial variation of those quantities along the run and branch).

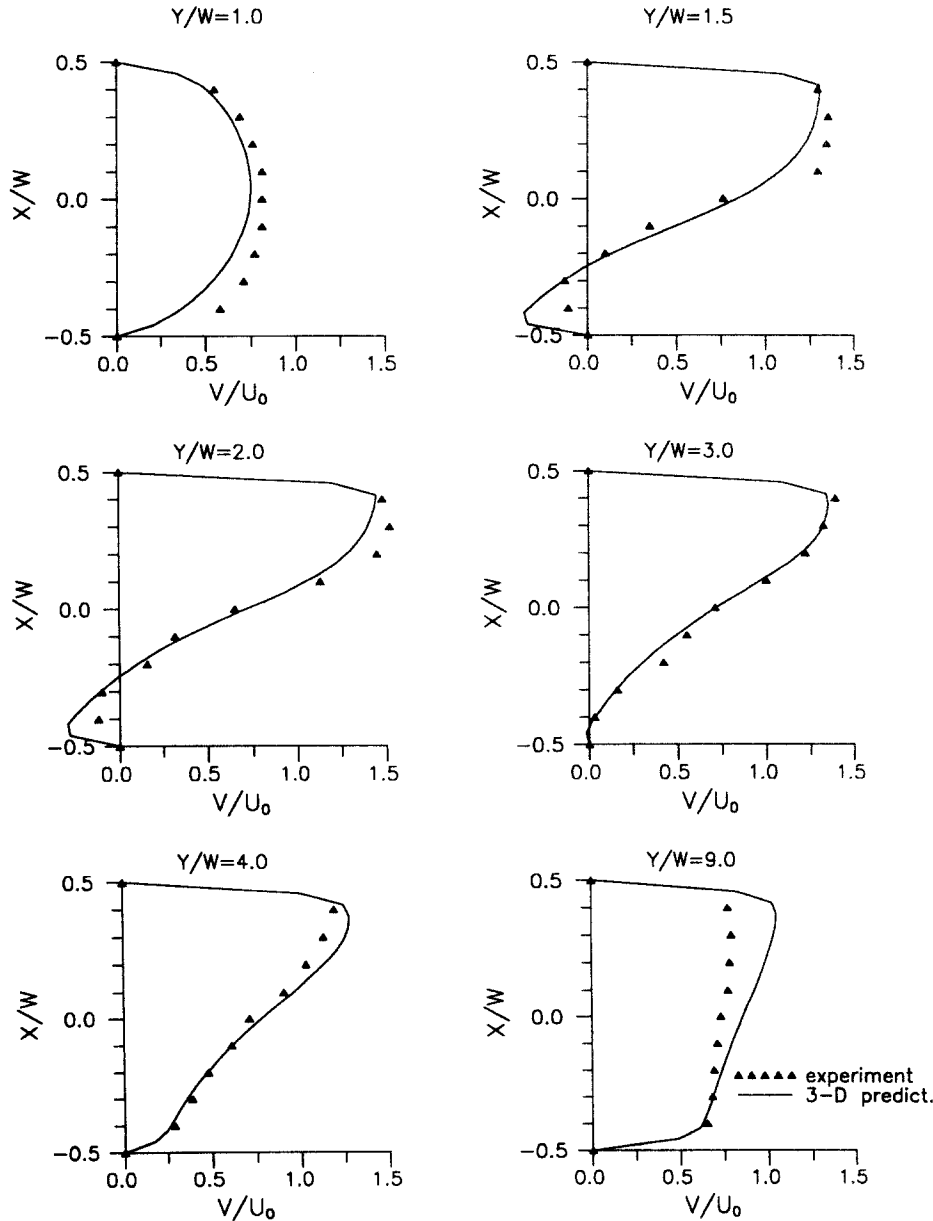


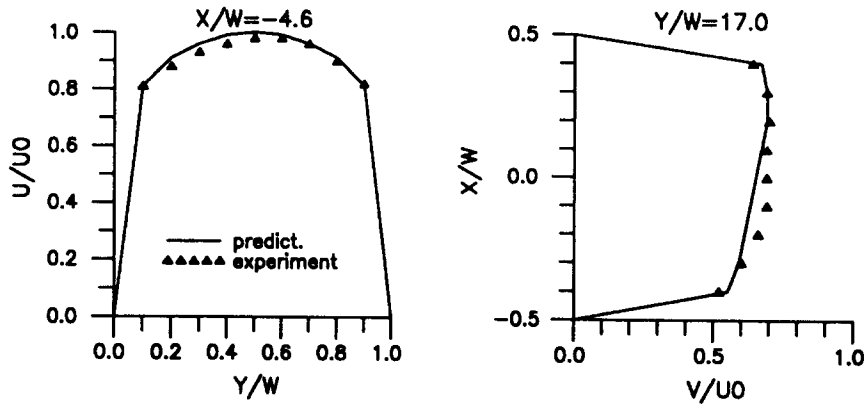
Fig. 5(b)

Fig. 5. Comparison of predicted velocity profiles with Popp and Sallet's [16] data for single-phase flow: (a) branch; (b) run.

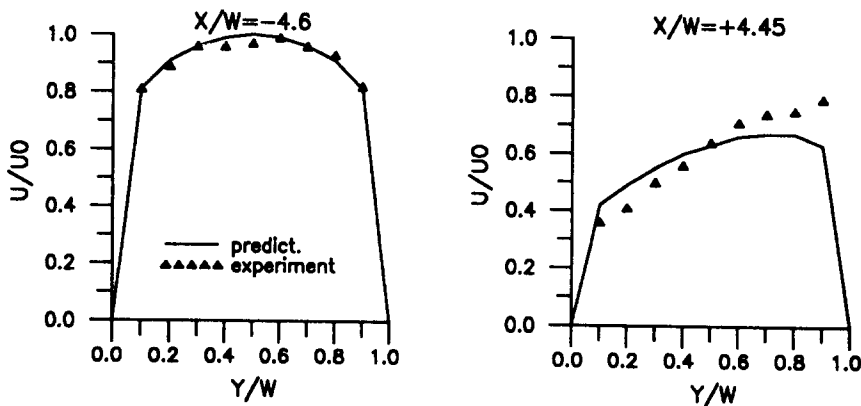
The number of time steps necessary for the normalized residuals of all equations to fall below 10^{-4} for the two-phase computations was around 3500 for a first run (from a single-phase solution) and 1500 for additional ones (restarting from a solution for a different Q_3/Q_1). Figure 4 presents typical decay of mass residuals along the pseudo-time-marching advancement for single- and two-phase runs ($Q_3/Q_1 = 0.7$), both started from uniform initial fields for all variables. The single-phase flow case converges five times faster, for the particular situation shown.

Velocity Comparisons

Most of the LDA velocity measurements by Popp and Sallet were for single-phase water flow, with deflection ratios of 0.38 and 0.81. Detailed comparison of predicted and experimental velocity profiles is made in Fig. 5 for the case of $Q_3/Q_1 = 0.81$. The profiles are for stations located on the symmetry plane (which is the vertical plane located in mid-channel, $Z = 0$), along the branch and the run, where reverse flow occurs; coordinates are non-dimensional with respect to W and the origins can be seen in Fig. 7; velocities are non-dimensionalized by the maximum value at inlet (U_0). Figure 5 shows the predictions using three-dimensional calculations on the fine mesh. Velocity profiles in the branch are in good agreement with data, which is reflected in the match of predicted and measured recirculation lengths (X_R = distance from branch entrance to the liquid reattachment point), both being $2.1W$ (here, a two-dimensional calculation would overpredict X_R by 17%). In the run [Fig. 5(b)], the velocity profiles do not agree so well with the data for stations at the



a) $Q_3/Q_1 = 0.70$



b) $Q_3/Q_1 = 0.38$

Fig. 6. Comparison of predicted velocity profiles with Popp and Sallet's [16] data for two-phase flow: (a) $Q_3/Q_1 = 0.70$; (b) $Q_3/Q_1 = 0.36$.

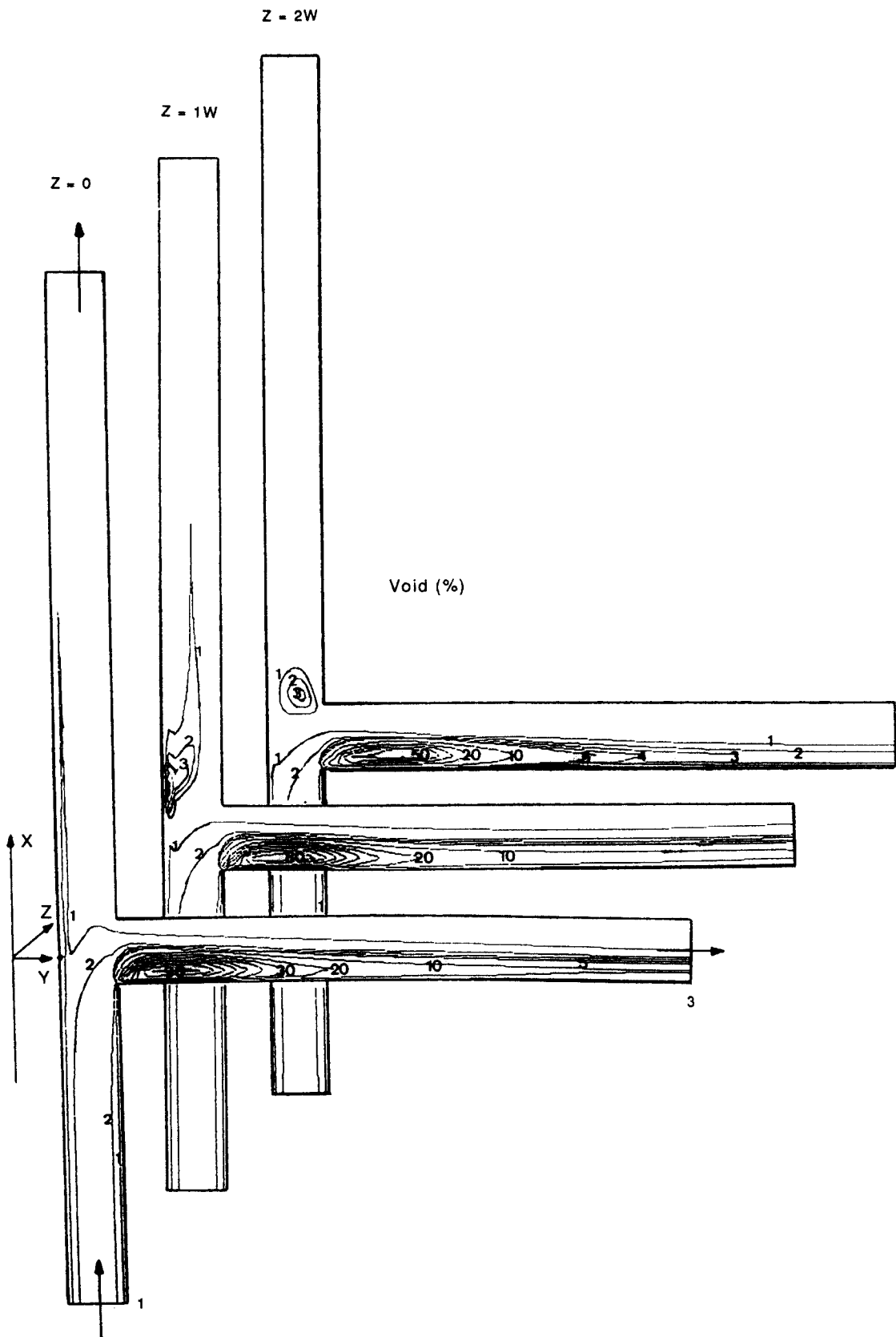


Fig. 7. Contours of void fraction at three planes of the three-dimensional field ($Q_3/Q_1 = 0.80$).

junction ($X \leq +0.5W$), but further downstream the recirculation zone in the run is well-captured, a feature which the two-dimensional calculations cannot produce (dotted lines). This is due to the strong secondary motions, creating a local zone of three-dimensional flow, as mentioned earlier.

Popp and Sallet [16] provide only a few profiles for the water velocity in two-phase flow; these hardly differ from their single-phase counterpart. The measurement stations are situated at the

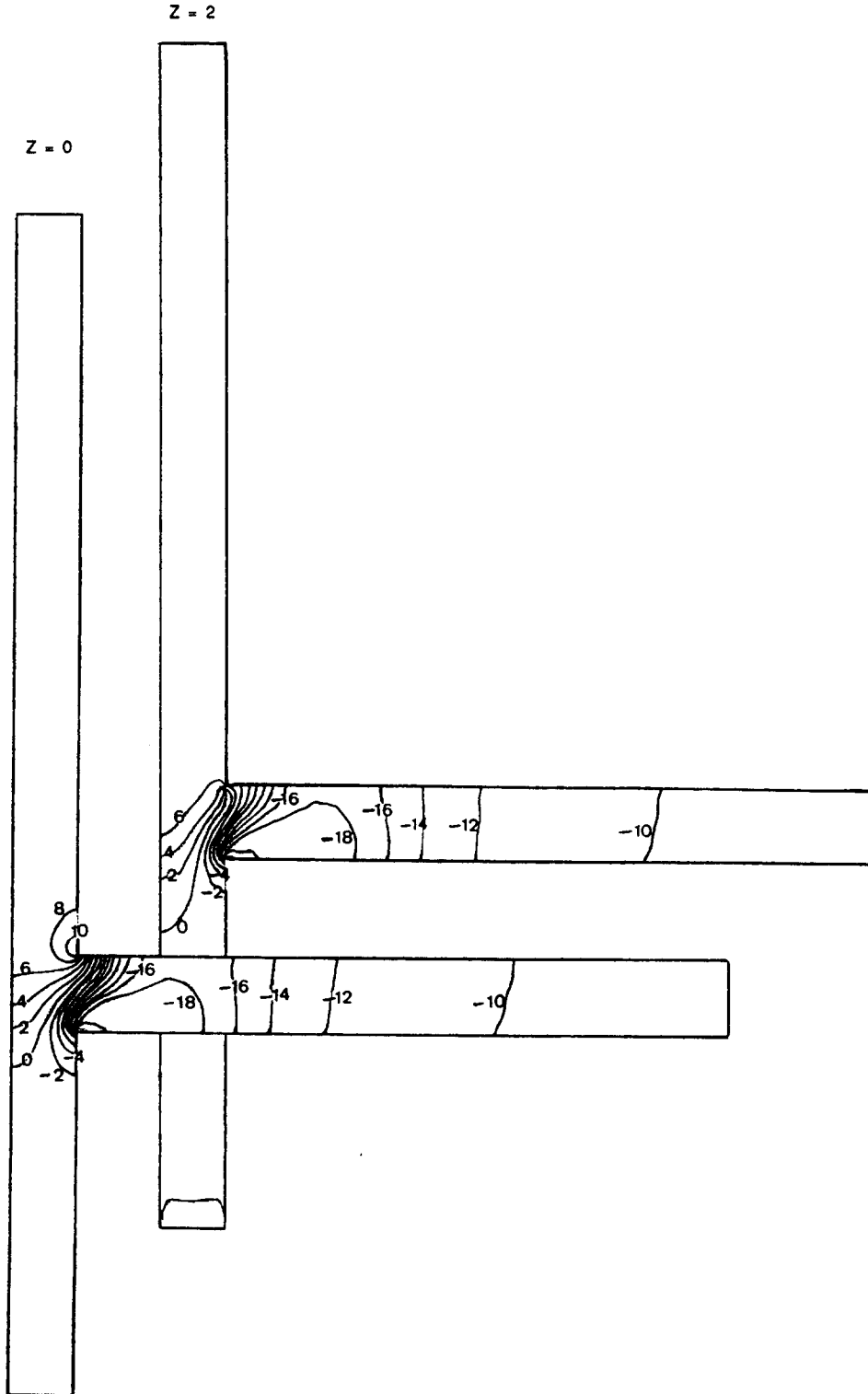


Fig. 8. Contours of pressure ($P \times 10^2 \text{ N/m}^2$) at the near-wall ($Z = 2$) and the symmetry plane ($Z = 0$), $Q_3/Q_1 = 0.80$.

outlet of the branch ($Y = 17W$) and outlet of the run ($X = 4.45W$); the data are compared with the present predictions in Fig. 6. For these predictions, the computational branch length was extended to $L_3 = 20W$, in order to obtain the profile at $Y = 17W$. It can be seen, for the case of $Q_3/Q_1 = 0.70$, that the measured velocity profile at the branch outlet is almost developed, whereas the predicted one is still recovering (although differences are small). This situation would in fact also happen in single-phase predictions, and is a known defect of the $k-\epsilon$ turbulence model [39].

The good agreement between predictions and data shown in these figures lends support to the two phase calculations considered next.

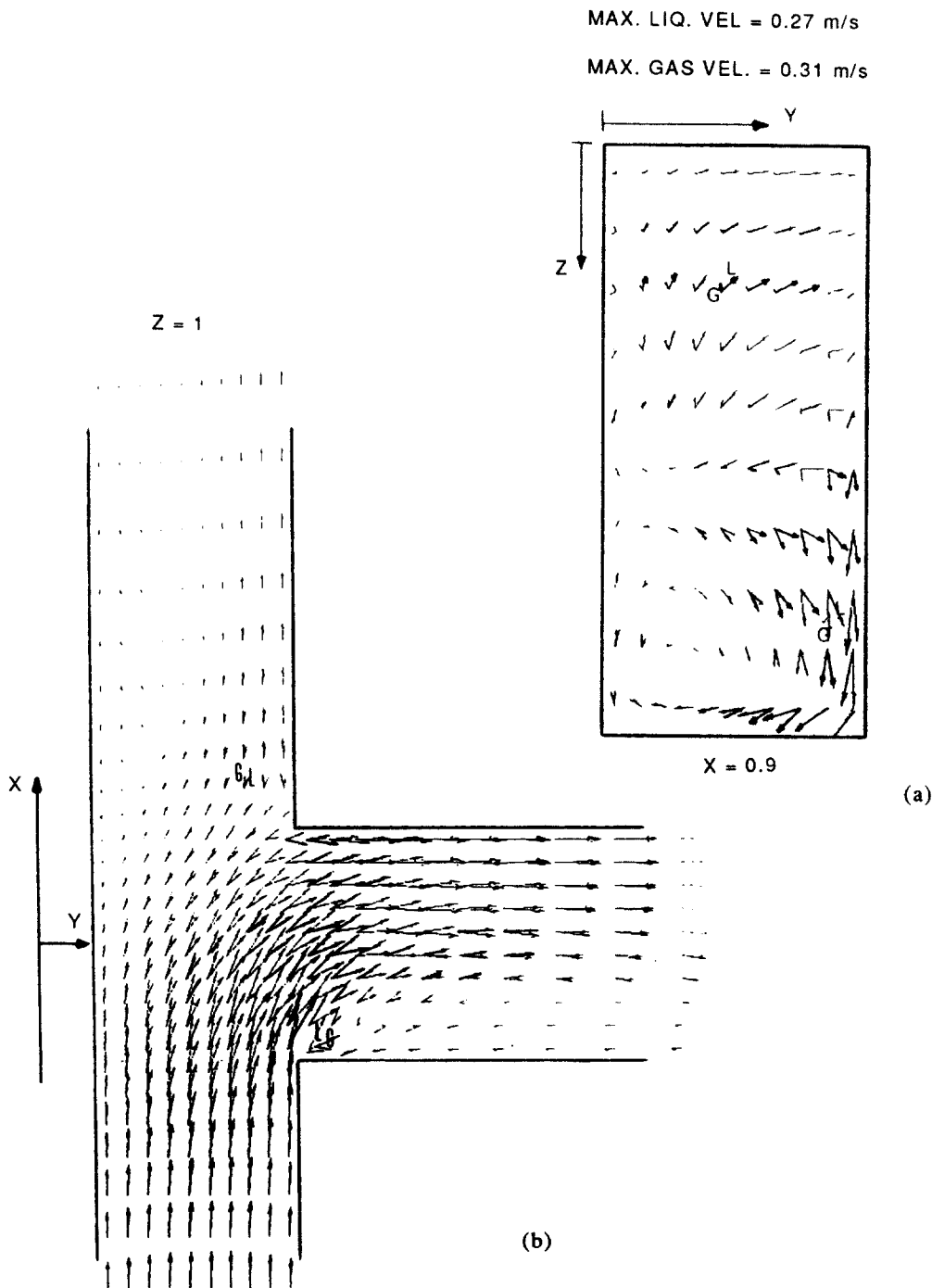


Fig. 9. Gas and liquid velocity vectors at two planes: (a) cross-stream plane, $X = 0.9$, (b) main flow plane, $Z = 1$.

Structure of the Two-phase Flow

In Fig. 7, gas volume-fraction contours are presented at three planes of the three-dimensional field: the mid-plane or symmetry plane ($Z = 0$); the near-wall plane ($Z = 2W$); and a plane in between ($Z = W$). For the case considered ($Q_3/Q_1 = 0.80$), pressure forces at the junction are strong enough to provide almost complete separation of the gas, forming pockets at the entrance to the side branch as observed in photographs of the flow [16]. These air pockets at the lower-pressure side of the entrance to the side branch are predicted by the model (Fig. 7) with the void-fraction attaining maximum values of 97.8% for the plane $Z = 0$, and 89.1% for the near-wall plane. Such high values mean that the pockets contain gas almost exclusively. Some concentration of gas can also be noticed at the entrance to the run, close to the end wall, and in the middle plane, close to the wall at $Y = 0$; this results from the trapping of low momentum gas, flowing close to the walls, by the strong adverse pressure field. Part of the gas will also be trapped in the recirculation zone existing downstream in the run, opposite to the side arm. The pressure contours shown in Fig. 8 illustrate the mechanism responsible for creating the slip between the two phases.

One of the advantages of the present multidimensional approach is the ability to study the detailed behaviour of the flow field in regions of interest. In this case, it is of interest to examine the velocity field of both phases in the region of intersection of the T-junction. Figure 9 shows gas and liquid velocity vectors in the planes $X = 0.6W$ perpendicular to the main flow direction, and $Z = W$, which is the longitudinal middle plane, where gas pockets occur in the branch and in the opposite side of the run. Departure in the direction of the different phase velocity vectors is a manifestation of the three-dimensional slip setup which is the cause behind phase segregation.

Phase Separation

For the quantitative validation of the two-phase flow predictions, other than the few velocity profiles in Fig. 6, only overall quantities are available in the published literature, namely: outlet-to-inlet gas and liquid flow rate ratios. Hence, several computational runs are required where

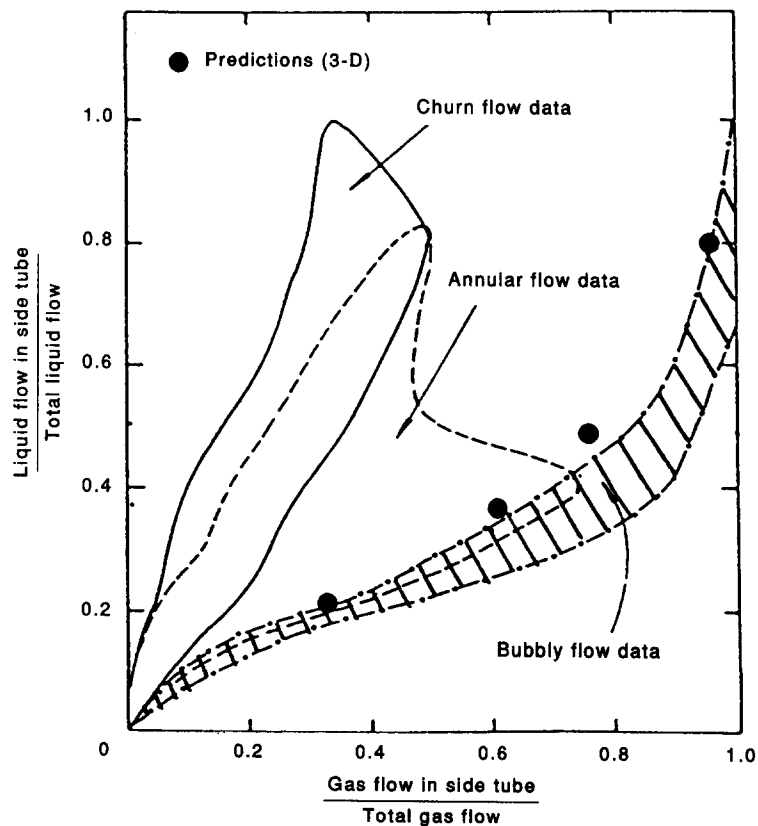


Fig. 10. Phase separation ratios: predictions and data.

Table 3. Flow rates and void-fraction as a function of the extraction ratio

| Q_3/Q_1 | $(Q_2)_G$ | $(Q_3)_G$ | $(Q_2)_L$ | $(Q_3)_L$ | α_2 [%] | α_3 [%] |
|-----------|-----------|-----------|-----------|-----------|----------------|----------------|
| 0.20 | 2.776 | 1.357 | 1.513 | 0.372 | 1.75 | 4.35 |
| 0.38 | 1.626 | 2.507 | 1.178 | 0.707 | 1.35 | 4.22 |
| 0.50 | 1.010 | 3.126 | 0.953 | 0.932 | 1.06 | 4.02 |
| 0.80 | 0.175 | 3.960 | 0.384 | 1.502 | 0.42 | 3.05 |

$Q_G, 10^{-5} [\text{m}^3/\text{s}]; Q_L, 10^{-3} [\text{m}^3/\text{s}].$

the imposed total extraction ratio Q_3/Q_1 is varied in steps (0.2, 0.38, 0.5 and 0.8). In Fig. 10 the rate of flow of gas into the side arm as a function of the total gas flow rate $(Q_3/Q_1)_G$ is plotted against the corresponding ratio of the liquid phase $(Q_3/Q_1)_L$. Agreement with the data for the bubbly flow regime (shown by the hatched area in the figure) from Ref. [2] is remarkable. It is noteworthy that for the present geometry, where the T-junction is formed from rectangular cross-section channels of 4/1 aspect ratio, the phase separation results using two-dimensional computations [40] are close to those obtained here. Computed average values of gas and liquid volumetric flow-rates and void-fraction at outlets 2 and 3 (run and side branch) are given in Table 3. Notice how the average void-fraction in the side-arm outlet is always greater than the corresponding one in the straight arm. Also noteworthy are the almost identical values of Q_3/Q_1 and $(Q_3/Q_1)_L$, resulting from the low void-fractions and high density ratio ($\rho_L/\rho_G = 1000/1.2$), which imply very low qualities.

Performance of the Turbulence Models

The extended two-phase turbulence model described earlier is based on the premise that the void-fraction fluctuates like all other quantities [28]. The model leads to the introduction of many additional terms, in both the momentum and the k and ϵ equations. These terms need modelling and have proved to be troublesome numerically. Here a study in which the additional terms are omitted (which would amount to ignoring the fluctuations in void fraction on turbulence) is presented.

For a deflection ratio of $Q_3/Q_1 = 0.38$, Figs 11(a) and (b) show contours of the void-fraction in the mid-plane when the extra turbulence-model terms [equations (16), (17), (20) and (21)] are omitted and included, respectively. The effect of the terms is to smooth the gradients of α close to the walls and at the edge of the gas pocket, in the side-arm entrance. In terms of the phase separation ratio, the effect is almost negligible, with $(Q_3/Q_1)_G$ decreasing by only 3%, as Table 4 shows.

Unfortunately it is not possible to deduce from the available experimental results for T-junction flows whether the more complex model gives better predictions. Proper assessment of the improved model has to be left to the predictions of simpler flows, e.g. flows in vertical channels and pipes, for which there exist local measurements of velocities and void-fraction.

Effect of the Drag Force Expression

The drag coefficient correction factor $f(\alpha)$ was taken as $f(\alpha) = 1 - \alpha$ as a base case. Table 5 and Fig. 11(c) provide an indication of the effect of taking the drag factor to be $f(\alpha) = 1/(1 - \alpha)^2$, which accounts for the increase in drag to bubble interactions at high void-fractions, for $Q_3/Q_1 = 0.38$.

Basically, the new factor does not affect the phase separation ratio, which is determined from conditions at and upstream of the junction; this is because there the void-fractions are small, so $f(\alpha) \simeq 1$, and the phase fraction contours follow identical paths, as in Fig. 11(a). However, there is a noticeable effect on the gas pocket in the side arm, where the tendency is for the pocket to become smaller, with lower maximum void-fraction in the symmetry plane $Z = 0$ (70% instead of 97%); this is a consequence of the stronger coupling between the phases since drag is higher. The length of the recirculation zone X_R is therefore decreased, from 4.8 (base case) to 3.6W, on

Table 4. Effect of the turbulence model

| Parameter | $(Q_3/Q_1)_G$ | $\langle \alpha \rangle_3$ | $\langle p \rangle_3$ |
|--------------------------|---------------|----------------------------|-----------------------|
| Base case (simple model) | 0.61 | 4.2 | -185 |
| Extended model | 0.59 | 3.3 | -164 |

$p, [\text{N}/\text{m}^2]; \alpha, [\%].$

Table 5. Effect of the drag corrective factor, $f(\alpha)$

| Parameter | $(Q_3/Q_1)_G$ | $\langle \alpha \rangle_3$ | $\langle p \rangle_3$ |
|-------------------------------------|---------------|----------------------------|-----------------------|
| Base case | 0.61 | 4.2 | -185 |
| With $f(\alpha) = 1/(1 - \alpha)^2$ | 0.60 | 3.9 | -175 |

$p, [\text{N}/\text{m}^2]; \alpha, [\%].$

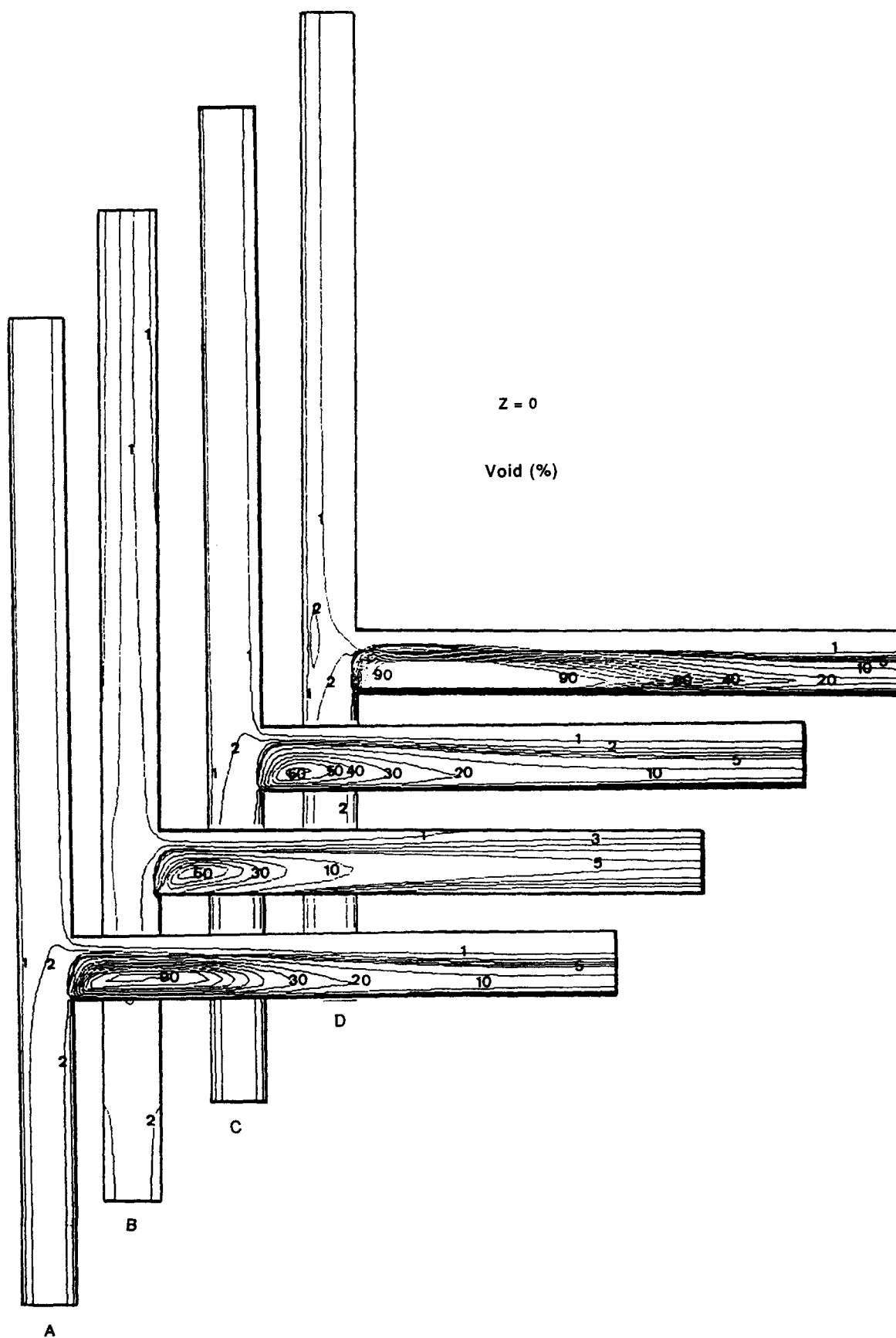


Table 6. Effect of the bubble diameter

| Parameter | $(Q_3/Q_1)_G$ | $\langle \alpha \rangle_3$ | $\langle p \rangle_3$ |
|-------------------|---------------|----------------------------|-----------------------|
| Base case | 0.61 | 4.2 | -185 |
| Bubble dia = 3 mm | 0.84 | 6.1 | -225 |

p , [N/m²]; α , [%].

the symmetry plane. Whether inclusion of the factor improves the predictions should be based on a comparison of the predicted X_R with measurements; unfortunately, such a measurement is not provided by Popp and Sallet [16] for two-phase flows.

Effect of Bubble Diameter

In the absence of information on the value of the bubble diameter in the experiments with which comparisons have been made, a diameter of 1 mm for the bubbles was assumed in the computations. This is reasonable in view of the low void-fraction cases considered. Here, an investigation into the sensitivity of the results to that value is undertaken. Figure 11(d) shows the void-fraction contours when the bubble diameter is taken as 3 mm, instead of the 1 mm value which was used throughout as a base case. It can be observed that the extension of the gas pocket in the side arm is greatly increased and that, this time, this corresponds to a higher separation of gas (see Table 6 for the case of $Q_3/Q_1 = 0.38$).

The effect of larger bubble diameter is to reduce the drag coefficient [equations (6) and (7)] so that the gas will tend to respond more readily to the pressure gradients at, and in the junction. In fact, inspection of Figs 11(a) and (d) shows that the contour of $\alpha = 2\%$ turns more sharply into the side arm when $d_b = 3$ mm, indicating that more gas is being drawn into that arm. Table 6 also shows that the pressure drop in the branch is higher for this case, which is a consequence of the extended recirculation zone ($X_R = 5.1W$). It is worth noting that the higher separation predicted with $d_b = 3$ mm is actually closer to the experimental data than that obtained with 1 mm.

CONCLUSIONS

The paper presents a three-dimensional approach to the prediction of two-phase flow in T-junctions. The method was first applied to single-phase three-dimensional flow through T-junctions; the results are in very good agreement with the experimental data. It was then applied to the two-phase bubbly flow of air and water through similar geometries. The predicted separation is in remarkable agreement with the published data.

Among the parameters studied, the one which greatly affects the degree of phase separation is the bubble diameter: an increase in d_b provokes more gas to be drawn into the side arm as a consequence of the decrease in drag. The extended turbulence model and the different forms of the drag coefficient relationship affect only the local extension of the gas pocket in the side arm and the structure of the flow in that region, but not $(Q_3/Q_1)_G$.

Future development will need to address several questions and introduce many refinements. Among these are the extension of the method to flow regimes other than bubbly flow and further testing and tuning of the modified turbulence model which is supposed to account for two-phase effects properly.

Acknowledgements—This work was carried out with the financial support of Marine Technology Directorate Ltd, England.

REFERENCES

1. W. Seeger, J. Reiman and U. Muller, Two-phase flow in a T-junction with a horizontal inlet. Parts I and II. *Int. J. Multiphase Flow* **12**, 575 (1986).
2. B. J. Azzopardi and P. B. Whalley, The effect of flow patterns on two-phase flow in a T junction. *Int. J. Multiphase Flow* **8**, 491 (1982).
3. B. J. Azzopardi and A. Purvis, Measurements of the split of a two-phase flow at a vertical T junction. Reports AERE R12441 and HTFS RS 720, Harwell, England (1987).
4. S. T. Hwang, H. M. Soliman and R. T. Lahey Jr, Phase separation in dividing two-phase flows. *Int. J. Multiphase Flow* **14**, 439 (1988).
5. B. J. Azzopardi, The effect of the side arm diameter on the two-phase split at a T-junction. *Int. J. Multiphase Flow* **10**, 509 (1984).
6. R. T. Lahey Jr, Current understanding of phase separation mechanisms in branching conduits. *Nucl. Engng Des.* **95**, 145 (1986).

7. B. J. Azzopardi and A. Memory, The split of two-phase flow at a horizontal T—annular and stratified flow. Presented at the 4th Int. Conf. on Multiphase Flow, Nice, France (1989).
8. B. J. Azzopardi and P. A. Smith, Two-phase flow split at T-junctions with horizontal and vertically upward side arms. Presented at the Int. Conf. of Basic Principles and Industrial Applications of Multiphase Flow, IBC, London (1990).
9. T. J. Honan and R. T. Lahey Jr, The measurement of phase separation in wyes and tees. *Nucl. Engng Des.* **64**, 93 (1981).
10. N. Saba and R. T. Lahey Jr, The analysis of phase separation phenomena in branching conduits. *Int. J. Multiphase Flow* **10**, 1 (1984).
11. Y. Taitel and A. E. Dukler, A model for predicting flow regime transitions in horizontal and near horizontal gas–liquid flow. *AIChE JI* **22**, 47 (1976).
12. Y. Taitel, D. Barnea and A. E. Dukler, Modelling flow pattern transitions for steady upward gas–liquid flow in vertical tubes. *AIChE JI* **26**, 345 (1980).
13. R. T. Lahey Jr, Dividing flow in a tee junction (data set No. 9). In *Multiphase Science and Technology* (Edited by G. F. Hewitt *et al.*), Vol. 3, p. 316 (1987).
14. J. D. Ballyk, M. Shoukri and A. M. Chan, Steam–water annular flow in a horizontal dividing T-junction. *Int. J. Multiphase Flow* **14**, 265 (1988).
15. M. T. Rubel, H. M. Soliman and G. E. Sims, Phase distribution during steam–water flow in a horizontal T-junction. *Int. J. Multiphase Flow* **14**, 425 (1988).
16. M. Popp and D. W. Sallet, Experimental investigation of one- and two-phase flow through a tee-junction. Presented at the Int. Conf. on Physical Modelling of Multiphase Flow, Coventry, England (1983).
17. M. R. Davis and B. Fungtamasan, Two-phase flow through pipe branch junctions. *Int. J. Multiphase Flow* **16**, 799 (1990).
18. G. E. McCreery and S. Banerjee, Phase separation of dispersed mist and dispersed annular (rivulet and thin film) flow in a tee—I. Experiments. *Int. J. Multiphase Flow* **16**, 429 (1990).
19. A. E. Fouda and E. Rhodes, Two phase annular flow stream division in a simple tee. *Trans. Instn Chem. Engrs* **52**, 354 (1974).
20. J. G. Collier, from Ref. [6].
21. K. C. Hong, Two-phase flow splitting at a pipe tee. *J. Pipeline Technol.* **30**, 290 (1978).
22. J. A. R. Henry, Dividing annular flow in a horizontal tee. *Int. J. Multiphase Flow* **7**, 343 (1981).
23. P. B. Whalley and B. J. Azzopardi, Two-phase flow in a 'T' junction. Report AERE R9699, Harwell, England (1980).
24. B. J. Azzopardi and S. R. Baker, Two-phase flow in a T junction: the effect of flow pattern in vertical upflow. Report AERE R10174, Harwell, England (1981).
25. B. J. Azzopardi and G. Freeman-Bell, The effect of side arm diameter on the two phase flow split at a T-junction. Report AERE M3290, Harwell, England (1983).
26. M. Ishii, *Thermo-fluid Dynamic Theory of Two-phase Flow*. Eyrolles, Paris (1975).
27. N. Zuber, On the dispersed two-phase flow in the laminar flow regime. *Chem. Engng Sci.* **19**, 897 (1964).
28. A. D. Gosman, R. I. Issa, C. Lekakou, M. K. Looney and S. Politis, Multidimensional modelling of turbulent two-phase flows in stirred vessels. *AIChE JI* **38**, 1853 (1992).
29. S. Politis, Prediction of two-phase solid–liquid turbulent flow in stirred vessels. Ph.D. Thesis, Imperial College, Univ. of London (1989).
30. B. E. Launder and D. B. Spalding, *Mathematical Models of Turbulence*. Academic Press, London (1972).
31. C. M. Rhie and W. L. Chow, Numerical study of the turbulent flow past an airfoil with trailing edge separation. *AIAA JI* **21**, 1525 (1983).
32. A. Pollard and D. B. Spalding, On the three-dimensional laminar flow in a tee-junction. *Int. J. Heat Mass Transfer* **23**, 1605 (1980).
33. S. V. Patankar and D. B. Spalding, A calculation procedure for heat, mass and momentum transfer in three-dimensional parabolic flows. *Int. J. Heat Mass Transfer* **15**, 1787 (1972).
34. I. Ellul and R. I. Issa, Prediction of the flow of interspersed gas and liquid phases through pipe bends. *Chem. Engng Res. Des.* **65**, Jan (1987).
35. M. Peric, A finite volume method for the prediction of three-dimensional fluid flow in complex geometries. Ph.D. Thesis, Imperial College, Univ. of London (1985).
36. R. I. Issa, Cell-face velocities on non-staggered meshes. Internal Note, Imperial College, Univ. of London (1986).
37. P. J. Oliveira, Computer modelling of multidimensional multiphase flow and application to T-junctions. Ph.D. Thesis, Imperial College, Univ. of London (1992).
38. R. I. Issa, Solution of the implicitly discretized fluid flow equations by operator-splitting. *J. Comput. Phys.* **62**, 40 (1986).
39. B. E. Launder, W. C. Reynolds and W. Rodi, *Turbulence Models and Their Application*, Vol. 2. Eyrolles, Paris (1984).
40. R. I. Issa and P. J. Oliveira, A multidimensional approach to the prediction of two-phase flow in T-junctions. Presented at the Int. Conf. of Basic Principles and Industrial Applications of Multiphase Flow, IBC, London (1990).
41. S. G. Bankoff, A variable density single-fluid model for two-phase flow with particular reference to steam–water flow. *Trans. ASME JI Heat Transfer* **82**, 265 (1960).

APPENDIX

Derivation of the Pressure-correction Equation

The steps required to derive the pressure-correction equation for two-phase flows, in a pseudo-time-marching algorithm and using non-staggered mesh, are as follows.

1. Compute fluxes for both phases using equation (41), based on starred velocities, U^* :

$$F_k^* = \frac{1}{A_{p,f}} \left\{ \left(\frac{\alpha_c \rho_c \gamma}{\delta t} \right)^f F_{fc}^* + \tilde{\alpha}_c^f \rho_c \sum_i B_{fi}^f \left(A_{pi}^{uc} U_{ci}^{*p} + \alpha_c^p B_{fi}^p [\Delta p^n]_f^p - \left(\frac{\alpha_c \rho_c \gamma}{\delta t} U_{ci}^n \right)^f - \tilde{\alpha}_c^f B_{fi}^f [\Delta p^n]_f^f \right) \right\} \quad (A1)$$

and

$$F_{fd}^* = \frac{1}{A_p^{ucf}} \left\{ \left(\frac{\alpha_d \rho_d \mathcal{V}}{\delta t} \right)^f F_{fd}^n + \tilde{\alpha}_d^f \rho_d \sum_i^3 B_i^f \left(A_p^{uc} U_{di}^* + \alpha_d^p B_i^p [\Delta p^n]_i^p - \left(\frac{\alpha_d \rho_d \mathcal{V}}{\delta t} U_{di}^n \right)^f - \tilde{\alpha}_d^f B_i^f [\Delta p^n]_i^f \right) \right\}. \quad (A2)$$

The only difference between these two equations, except for the continuous and dispersed phase subscripts, is the central coefficient of the respective momentum equations. From equations (47) and (48) it can be seen that

$$A_p^{uc} = A_0^c + \frac{\alpha_c \rho_c \mathcal{V}}{\delta t} = A_0^c + A'^c$$

and

$$A_p^{ud} = A_0^d + \frac{\alpha_d \rho_d \mathcal{V}}{\delta t} + F_D = A_0^d + A'^d,$$

where $A' \equiv A_p - A_0$.

2. Splitting of the continuous phase momentum equation (following Issa's [38] ideas):

$$\frac{\alpha_c \rho_c \mathcal{V}}{\delta t} U_{ci}^{n+1} = H_c^n(U_{ci}^*) - A_0^c U_{ci}^* - \alpha_c^p \sum_i^3 B_i^p [\Delta p^{n+1}]_i^p + F_D(U_{ci}^n - U_{ci}^*) + S_{ui}^c + \frac{\alpha_c \rho_c \mathcal{V}}{\delta t} U_{ci}^n. \quad (A3)$$

3. Splitting of the dispersed phase momentum equation:

$$\left(\frac{\alpha_d \rho_d \mathcal{V}}{\delta t} + F_D \right) U_{di}^{n+1} = H_d^n(U_{di}^*) - A_0^d U_{di}^* - \alpha_d^p \sum_i^3 B_i^p [\Delta p^{n+1}]_i^p + F_D U_{ci}^* + S_{ui}^d + \frac{\alpha_d \rho_d \mathcal{V}}{\delta t} U_{di}^n. \quad (A4)$$

4. Correction equation for continuous phase nodal velocity, subtract equation (A3) from equation (47) to obtain:

$$\frac{\alpha_c \rho_c \mathcal{V}}{\delta t} (U_{ci}^{n+1} - U_{ci}^*) = -\alpha_c^p \sum_i^3 B_i^p [\Delta(p^{n+1} - p^n)]_i^p. \quad (A5)$$

5. Correction equation for dispersed phase nodal velocity, subtract equation (A4) from equation (48) to obtain:

$$\left(\frac{\alpha_d \rho_d \mathcal{V}}{\delta t} + F_D \right) (U_{di}^{n+1} - U_{di}^*) = -\alpha_d^p \sum_i^3 B_i^p [\Delta(p^{n+1} - p^n)]_i^p. \quad (A6)$$

6. Splitting and correction equations for the fluxes; this derivation follows closely that for the nodal (center of cell) velocities given above and so only the final correction equations are given. In the splitting process, only the last Δp terms of equations (A1) and (A2) are updated to Δp^{n+1} , so that after the subtraction the following results:

$$F_{fc}^{n+1} - F_{fc}^* = -\frac{1}{A_p^{ucf}} \left\{ \tilde{\alpha}_c^f \rho_c \sum_i^3 B_i^f \tilde{\alpha}_c^f B_i^f [\Delta(p^{n+1} - p^n)]_i^f \right\} = -\frac{1}{A_p^{ucf}} \tilde{\alpha}_c^f \rho_c B_j^2 \tilde{\alpha}_c^f [\Delta p]_j^f,$$

where $p' \equiv p^{n+1} - p^n$, the area of face f is $B_f(\Sigma_i B_i^f \cdot B_j^f)^{1/2}$ and, after dropping the superscript indicating where averages are taken, the final expression becomes:

$$F_{fc}^{n+1} = F_{fc}^* - \left(\frac{\tilde{\alpha}_c \tilde{\alpha}_c \rho_c}{A_p^{uc}} \right) B_j^2 [\Delta p]_j^f. \quad (A7)$$

Identically for the dispersed phase,

$$F_{fd}^{n+1} = F_{fd}^* - \left(\frac{\tilde{\alpha}_d \tilde{\alpha}_d \rho_d}{A_p^{ud}} \right) B_j^2 [\Delta p]_j^f. \quad (A8)$$

7. Pressure equation based on sum of the two continuity equations (42):

$$\sum_f^6 (-1)^f (F_{fc}^{n+1}/\rho_c + F_{fd}^{n+1}/\rho_d) = 0. \quad (A9)$$

After introducing equations (A7) and (A8) in this equation and regrouping the different terms, the pressure-correction equation (centered at point P) is obtained:

$$A_p^c p'_p = \sum_f A_f^c p'_f + S_u^c, \quad (A10)$$

where the coefficients and source term are given by

$$A_f^c = \left(\frac{\tilde{\alpha}_c \tilde{\alpha}_c}{A'^c} + \frac{\tilde{\alpha}_d \tilde{\alpha}_d}{A'^d} \right) B_j^2 \equiv A_{fc}^c + A_{fd}^c, \quad (A11)$$

$$A_p^c = \sum_f A_f^c \quad (A12)$$

and

$$S_u^c = -\sum_f^6 (-1)^f (F_{fc}^*/\rho_c + F_{fd}^*/\rho_d). \quad (A13)$$